Geochemical and textural evidence of eruption at Mt. St. Grégoire, Québec, or not

Alex Pernin

Professor James Brenan

2013

An undergraduate thesis submitted to the Department of Earth Sciences

University of Toronto, St. George Campus

Table of Contents

Abstract 4

Introduction 6

Overview 6

Previous Work 7

Geological Setting 8

Regional Geology 8

Local Geology 10

Methods and Materials 13

Sample Collection 13

Thin Section Procedure 13

Grain Mount Procedure 15

Electron Microprobe 20

Transmitted Light Microscope 20

Scanning Electron Microscope 21

Laser Ablation Inductively Coupled Plasma Mass Spectrometer 21

Results 23

Sample Mineral Abundances and Textures 23

Apatite Textures 30

Sample Geothermobarometry 32

Biotite Major and Minor Oxide Concentrations 35

Sample Trace Element Concentrations 36

Discussion 43

Evidence from Amphibole-Pyroxene Reaction Textures 44

Evidence from Geothermobarometry Calculations 45

Evidence from Biotite Oxide Concentrations 47

Evidence from Apatite and Biotite Trace Element Concentrations 52

Evidence from Volatile Element Concentrations 53

Conclusion 56

Acknowledgments 58

References 58

Abstract

Mt. St. Grégoire is a concentrically-zoned plug and the smallest of nine alkaline intrusions composing the Cretaceous-aged Monteregian Hills near Montreal, Québec. The Mt. St. Grégoire intrusion consists of an outer margin of porphyritic syenite and a core of aphanitic monzogabbro. Previous field interpretations described crystallization first occurring along the margins and progressing inwards towards the centre of the conduit with the intrusion hypothesized to have experienced eruptive degassing. The distinct reaction textures between amphibole and pyroxene across the intrusion have previously been presented as strong petrographical evidence of eruption at Mt. St. Grégoire; however, the texture essentially supports hydration of pyroxene to amphibole from the core to the margin of the intrusion. This indicates an increase in water fugacity conditions in the same direction rather than dehydration towards the centre. The oxygen fugacity values were calculated from the major and minor oxides in ulvöspinel-ilmenite exsolution and corresponded to a ΔNNO range of -1.44 to -2.04. Proposed degassing situations involving reduction from the evolution SO_2 or oxidation from hydration and consequent H_2 devolatilization cannot account for the absence of S-bearing mineral phases and the reduced state of the intrusion. Furthermore, major and minor oxide concentrations were measured in biotite across the intrusion. There is a progressive decrease of $\frac{MgO}{MgO+FeO}$ from the core unit to the margin which is explained by the natural differentiation of a primitive magma at the core to an evolved magma at the margin. The hydroxyl site atomic proportions of OH, Cl and F were also calculated. Considering the 10±1.5 partition coefficient between the aqueous fluid and the melt for Cl, hypothesized degassing would certainly be detectable in the variation between Cl and F or Cl and OH. However, the lack of any sequential decrease in Cl and especially the measured enrichment in Cl content in the coexisting melt at the core disprove the

volatile element readily leaving the system and provide definite evidence opposing degassing at Mt. St. Grégoire. Instead, the aphanitic texture in the core may be a result of crystallizing at a high degree of undercooling from the already-cooled marginal syenite rather than of a degassing scenario. Additionally, trace elements including Li, Cu, Rb, the REEs, Th and U were analysed in apatite and biotite. The compatible trace elements in apatite and biotite progressively decrease in abundance while volatile incompatible elements progressively increase in abundance from the core to the margin. This geochemical evidence represents the theoretically expected trends of fractionation in these various elements in the system and further supports the interpretation of Mt. St. Grégoire crystallizing from a primitive aphanitic monzogabbro at the core and a separate, non-continuous evolved nepheline syenite along the margins.

Introduction

Overview

Mt. St. Grégoire is the smallest of nine alkaline intrusions composing the Cretaceous-aged Monteregian Hills and is located 40km southeast of Montreal, Québec (Figure 1.1). The Mt. St. Grégoire intrusion is concentrically-zoned and consists of an outer margin of porphyritic syenite and a core of aphanitic monzogabbro. Beginning with Adams in 1903, several field descriptions and emplacement models have been proposed in order to explain the interesting lithologic differentiation although no hypothesis has been fully accepted, Philpotts (1968). Reasons for the ongoing controversy include no explanation accounting for the development of reverse zoning from a primitive core to a more evolved outer margin, the relation between the core and the margin as well as the aphanitic texture of the core rock type, Bédard (1989).

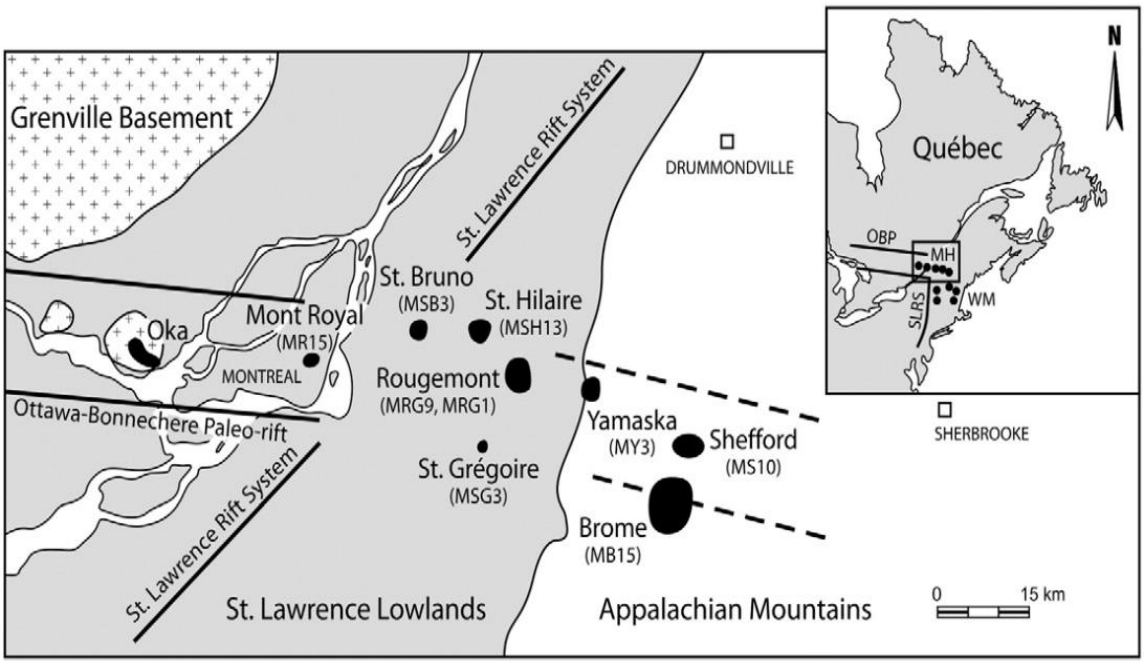

Figure 1.1: Location of the Monteregian Hills (MH) and Mt. St. Grégoire in Québec, modified from Roulleau et al. (2012).

The purpose of this thesis study was to collect and investigate the geochemical, compositional and textural evidence from Mt. St. Grégoire in order to resolve the popular hypothesis of the intrusion having experienced eruptive degassing. Petrographically, there is a progressive decrease in amphibole and a simultaneous increase in pyroxene from the Mt. St. Grégoire intrusion margin to the core which has been presented in the literature as evidence of dehydration. Grains of biotite, apatite, pyroxene, plagioclase and amphibole were analysed for any sequential loss of major, minor and trace volatile elements along the intrusion which may also support a degassing scenario. Moreover, Fe-Ti oxide geothermobarometry calculations were performed to provide information on ulvöspinel and ilmenite crystallization temperatures and on redox conditions indicating the magma type and any possible associations to devolatilization.

Previous Work

The Mt. St. Grégoire intrusion was first described by Adams (1903). His interpretations included the general igneous structures and the gradation in rock type from the margin to the core. Pajari (1967) also documented the geology in detail and released major and minor mineral oxide concentrations as well as other geochemical data. The experimental approach explaining the rock type differentiation used by Philpotts (1968) depended on two immiscible liquids convecting in a vertical pipe. Eby (1979) also proposed an emplacement sequence using two immiscible liquids. More recently, Roulleau et al. (2012) have investigated the magmatic sources of the Monteregian Hills using N, Ar and He isotopic compositions from amphiboles and pyroxenes across the intrusions. The authors concluded that there is contrasting evidence for either a plume or a depleted mantle component as the source of volcanism.

Geological Setting

Regional Geology

The Monteregian Hills follow an approximate E-W linear trend corresponding to the Ottawa-Bonnechere paleorift, a failed arm of the Iapetus Ocean, which extends from the Oka carbonatite complex and continues 80km eastward (Figure 1.1). Faults systems associated to the St. Lawrence graben and Beauharnois arch are assumed to be the controlling features responsible for the positions of these alkaline intrusions, Eby (1984). The Monteregian Hills are dated to 124±1.5Ma and were emplaced into three distinct geological terranes, Roulleau et al. (2012). Moving eastward, the Oka carbonatite complex intruded the Precambrian-aged Grenville Province gneiss and amphibolites. Mt. Royal, Mt. St. Bruno, Mt. St. Hilaire, Mt. Rougemont and Mt. St. Grégoire are located in the St. Lawrence Lowlands, a 500-1,000m thick sedimentary sequence consisting of Cambrian sandstone and Ordovician dolostones, carbonates and shales. The majority of Mt. Yamaska, the Mt. Shefford and the Mt. Brome intrusions were emplaced in quartzites, carbonates, slates and metamorphic rocks of the Appalachian Mountains, Eby (1984), Roulleau et al. (2012). Additionally, these terranes correspond to various silica saturation indices which are reflected in the intrusion compositions as indicated in Table 2.1.

Table 2.1: The silica saturation indices and mineral assemblages of the Monteregian Hills, Eby (1984), Roulleau et al. (2012)

Intrusion	**Silica Saturation Index**	**Mineral Assemblage**
Oka	Strongly silica-undersaturated	Carbonate
Mt. Royal	Slightly silica-undersaturated to moderately silica-oversaturated	Olivine, Ti-augite, amphibole, plagioclase
Mt. St. Bruno	Slightly silica-undersaturated to moderately silica-oversaturated	Olivine, plagioclase amphibole
Mt. St. Hilaire	Slightly silica-undersaturated to moderately silica-oversaturated	Pyroxene, amphibole, olivine
Mt. Rougemont	Slightly silica-undersaturated to moderately silica-oversaturated	Pyroxene, olivine, plagioclase
Mt. St. Grégoire	Slightly silica-undersaturated to moderately silica-oversaturated	Augite, hornblende, oligoclase, olivine
Mt. Yamaska	Slightly silica-undersaturated to moderately silica-oversaturated	Plagioclase, Ti-augite, hornblende
Mt. Shefford	Silica-oversaturated	Pyroxene, plagioclase, quartz, nepheline, hornblende
Mt. Brome	Silica-oversaturated	Plagioclase, clinopyroxene, hornblende, olivine

The intrusions are generally steep-sided, extend to great depths and were determined to have crystallized at relatively shallow crustal levels, Eby (1984). Using feldspar compositional data, the magmas were calculated to have been emplaced at pressures of 1kbar. Thus, the Monteregian Hills crystallized at depths around 2-3km below the Cretaceous surface, Eby (1984). Moreover, primary igneous textures and wall rock alteration from the high temperature

mafic melts indicate that crystallization first occurred along the margins and progressed inward towards the centre of the conduit, Eby (1984).

Local Geology

The Mt. St. Grégoire intrusion is approximately 750 long, 600m wide and the inner core rock type forming the summit is 120m above the surrounding Ordovician Lorraine siltstone. There are four lithologic units given in Figure 2.1: a core series separated into a porphyritic and an aphanitic oligoclase monzogabbro, a layered monzogabbro series and a porphyritic syenite peripheral series.

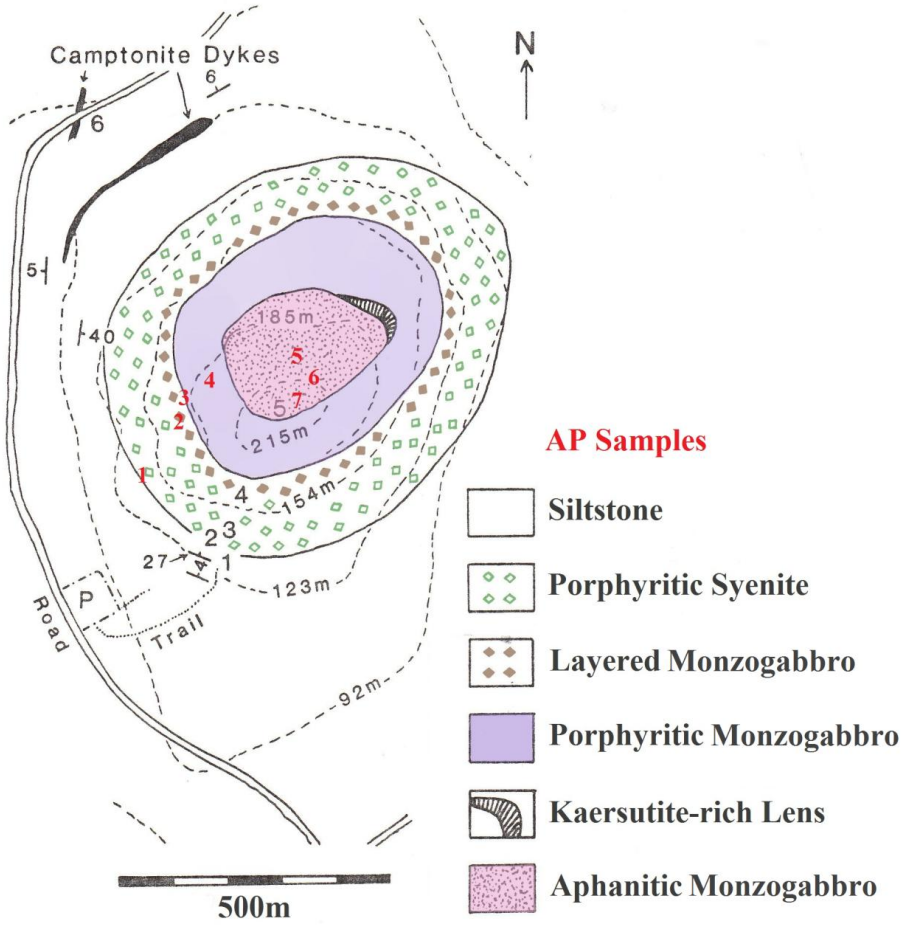

Figure 2.1: Geologic map of the Mt. St. Grégoire intrusion, modified from Bédard (1989).

The inner core aphanitic oligoclase monzogabbro has an average diameter of 240m. Bédard (1989), amongst others, has inferred this fine-grained texture as a quenched liquid, thus suggesting a degassing event. The contact with the porphyritic oligoclase monzogabbro is represented by a gradual increase in phenocryst abundance and groundmass grain size, Philpotts (1968). This outer core unit is roughly 100m thick and fully encircles the inner core unit. The well-layered cumulate monzogabbro surrounding the intrusion core is 50m thick. The rhythmic layers are prominent and are defined by alternating concentrations of felsic and ferromagnesian minerals, Philpotts (1968). These layers are concentric, vertically dipping, typically 10-20cm thick and laterally continuous on the m-scale, Bédard (1989). Also, a strong concentric foliation about the inner core is characterised by the vertical alignment of feldspar phenocrysts. This field evidence along with small trough-like primary igneous structures present within the layered series observed by Philpotts (1968) are interpreted as crystallization from the margins inward as well as a directional magma flow along the conduit margins. The peripheral series is composed of a 70m thick inner zone of porphyritic anorthoclase syenite, a transitional zone of 10m thick porphyritic biotite syenite and a marginal zone of 10m thick nepheline syenite. The feldspar phenocrysts are weakly aligned in this series possibly resulting from weak magma flow, Bédard (1989). The general mineral assemblage for the Mt. St. Grégoire intrusion includes feldspar, pyroxene, olivine (minor and only in the core series), amphibole, biotite, oxides, nepheline, sodalite (minor), apatite and titanite (minor and only in the layered and peripheral series). Regarding the country rock, the Ordovician Lorraine siltstone is metamorphosed to the hornblende hornfels facies along the intrusion. While the contact between the siltstone and the porphyritic nepheline syenite is not exposed, the horizontal siltstones are known to dip inwards concentrically surrounding Mt. St. Grégoire, Philpotts (1968). Figure 2.2 describes the

emplacement model interpreted by Bédard (1989). He believed that primitive hawaiite melt convected at the base of the magma chamber with a stable, evolved syenite magma above. The peripheral series then formed and crystallized on the conduit walls during the upward migration of the primitive melt with the internal flow represented by the layered unit. Lastly, the hawaiite was quenched from devolatilization on the surface as a volcano producing the aphanitic texture.

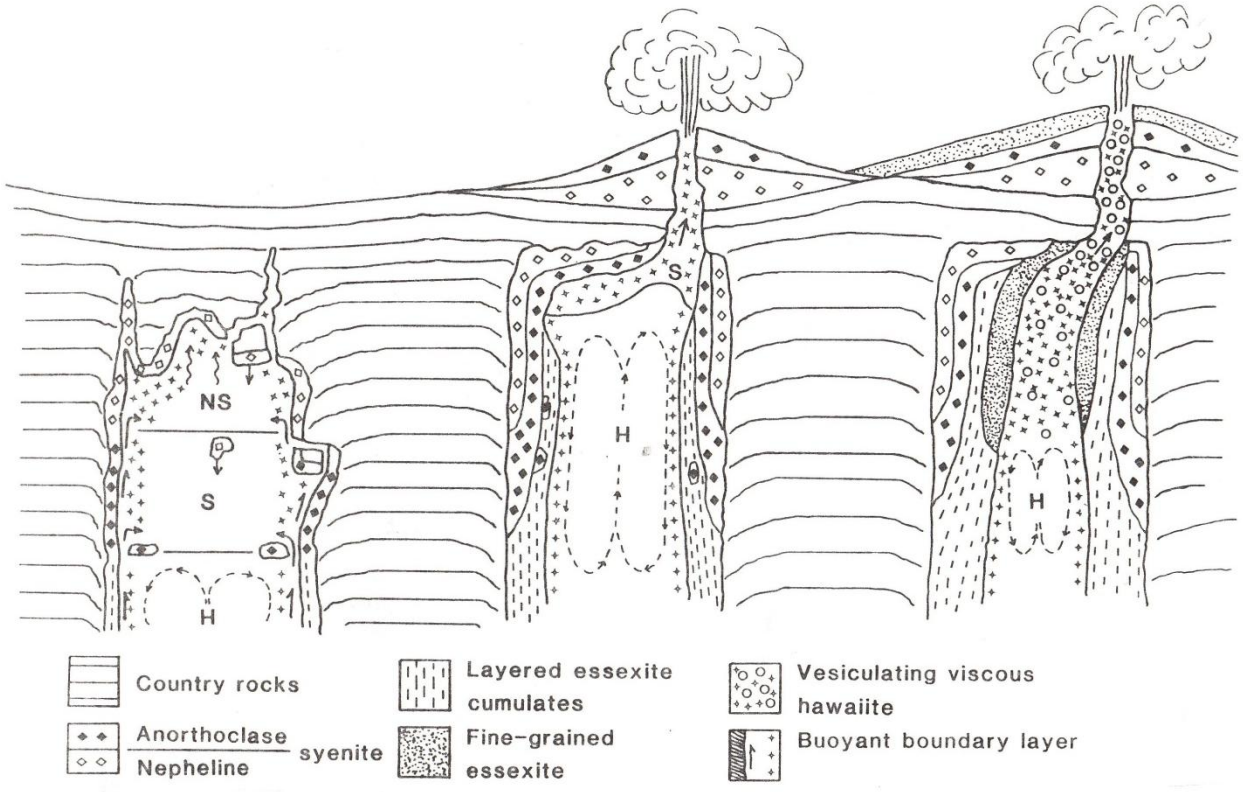

Figure 2.2: Interpretative emplacement model for the Mt. St. Grégoire intrusion, Bédard (1989).

Methods and Materials

Sample Collection

Hand samples were obtained on October 13, 2012 during the GLG318 field trip to the Monteregian Hills. Several representative samples were collected from each lithologic unit along the intrusion. The sample spacing was also determined by the occurrence of these units. The sample locations are given visually in Figure 2.1 and by coordinates in Table 3.1.

Table 3.1: Sample location coordinates along the Mt. St. Grégoire intrusion

Sample	**UTM Coordinate Location (m)** **Grid zone reference: 18T**
AP1	0644703 E 5024079 N
AP2	0644796 E 5024198 N
AP3	0644808 E 5024238 N
AP4	0644858 E 5024272 N
AP5	0645004 E 5024310 N
AP6	0645039 E 5024277 N
AP7	0645006 E 5024240 N

Once field observations of the surrounding lithology were made, the sample was removed from each respective outcrop using a rock hammer and chisel, was bagged and properly labelled and the GPS coordinates were then acquired using a Garmin Etrex Legend GPS.

Thin Section Procedure

Firstly, the hand sample was cut to approximate thin section dimensions using a Target diamond rock saw, allowed to dry and then labelled. The wide surface of the freshly cut slab was

ground down in a figure-8 pattern using various sanding papers. Sequentially, these papers were the 220b, 400 and 600 grit papers. 9μm and 1μm suspended solutions on polishing cloths were also used for final polishing. Once the surface was fully ground and smooth on a particular sand paper, the slab was rinsed and dried with compressed air before moving to the following grit size. Epoxy was prepared by mixing hardener and epoxy in a 4:10 ratio. The sample name was carved into a clean thin section with a diamond tip, epoxy was smeared onto the thin section and the polished surface of the slab was mounted onto the epoxy. The slab was then secured under a spring press against the thin section while simultaneously being heated by an underlying hot plate overnight.

Once the epoxy hardened, the cm-thick thin section was removed from the press and tightened into the Buehler IsoMet 4000 linear precision saw. The saw parameters used for trimming were 3000rpm and 0.6cm/min. Once the majority of the slab was removed, the edges and back surface of the thin section were cleaned and scraped using a razorblade to remove any excess epoxy. The following step required using the Buehler Petro-Thin thin section system to grind away at the thin section up to approximately 150μm. The equipment was originally not functional so the vacuum area was thoroughly scraped, cleaned and wiped to remove remaining debris from previous usage. The thin section was securely placed into the vacuum hold and the vacuum pump was set to 20 Hg. Starting at 100 units for the horizontal distance between the rock slab and the grinding plate, the thin section was carefully lowered into the thin sectioning system. The thin section was slowly ground multiple times, raised to decrease the distance by another 10 units and lowered once more. Grinding on this equipment continued until the arbitrarily chosen minimum distance of 30 units was reached. Throughout the process the thin section was removed from the vacuum seal and its thickness was measured using an imperial-

scaled calliper to confirm enough of the slab remained. The final step involved in the thin section preparation was polishing using the Buehler MetaServ 250 grinder-polisher. Four thin sections were placed onto holder platforms and secured into the overlying stage surface-down. The polisher parameters used were 250rpm and 7lbs of pressure pressed on each thin section. Polishing began using a 30μm diamond pad for 5-7 minutes to allow minor grinding and to attain the desired thin section thickness of 80μm. Once the thin sections were all ground and measured to the correct thickness, they were all rinsed and dried with compressed air. The 30μm pad was removed from the magnetic holder using a pick and 15μm suspended solution was then sprayed onto another grinding pad. The thin sections were tightened again into the stage and were polished for 15 minutes. This same cleaning and polishing process was repeated using a 9μm suspended solution and lastly using a 1μm suspended solution.

Grain Mount Procedure

Grain separation commenced with rock pulverization. Firstly, the workspace counter and table were wiped with a wet cloth to remove rock dust from any previous pulverization. Silica from glass bottle shards was poured into the tungsten carbide puck mill which was placed into a Rocklabs pulverizer for 40 seconds to clean and decontaminate the mill components. The silica was then disposed and the components along with the pouring spoon were rinsed, scrubbed with dish soap, dried and rinsed again with ethanol. Lily cups were obtained and several container bags were made by cutting and melting plastic. The hand sample was placed into a plastic bag, laid onto a steel impact platform and continuously smashed using a rock hammer. Once the plastic bag began to disintegrate, the resulting fragments were separated depending on size into two lily cups. The cup containing fragments larger than 2cm was emptied into a new plastic bag and this smashing process was repeated until the original sample consisted only of rock

fragments smaller than 2cm. The puck mill components were assembled on the table and 3 spoonfuls of rock fragments were poured into each half of the puck mill. The puck mill was carefully positioned and secured into the pulverizer and the pulverizer was turned on for 35 seconds. The puck mill was then removed from the pulverizer and the contained rock powder was slowly placed onto a clean sheet of paper. This paper was used to transfer the rock powder into a clean, labelled lily cup and the process was repeated until all sample fragments were pulverized into powder and placed into the lily cup.

The second step in grain separation required using the Wilfley table. The table was first thoroughly rinsed with a garden hose and nozzle, scrubbed with dish soap and rinsed again to prevent sample contamination. While the table partially dried by air, the Wilfley table attachments were removed from the 10% HCl container, rinsed with water and sonicated for 5 minutes. The 3 clamps and pouring spoon were rinsed with water and washed with dish soap. Once the Wilfley table attachments were sonicated, they were individually removed, rinsed with ethanol and all placed onto a clean sheet of paper. Before installing the attachments, a compressed air nozzle was used to remove any excess water and completely dry the table surface. The plastic distributor was clamped onto the top-right corner of the table below the water supply, the triangle splitter was clamped onto the bottom-left edge of the table and the final clamp was placed on the rotation dial to prevent the table from tilting. Two lily cups were also placed in the eavestrough under the triangle splitter to collect the light and heavy minerals for when the Wilfley table was on. Another lily cup was half filled with water and mixed with 2 spoonfuls of sample powder and 1 drop of dish soap to prevent any particle cohesion. Once the solution was mixed with the spoon, the water and Wilfley table vibrator were turned on and the solution was slowly poured into the distributor in increments of 3 spoonfuls every 2 minutes.

Additionally, the triangle splitter may have been moved laterally depending on the pathway of the light and heavy minerals. Once the original sample was completely separated and the Wilfley table surface was cleared of mineral grains, the lily cup containing the light minerals was reprocessed into the triangle splitter in increments of 3 spoonfuls every 45 seconds. Since the Wilfley table separation was preformed conservatively and heavy minerals were accidently dropped into the light mineral lily cup, this final separation was to correctly redistribute any apatite and biotite grains into the heavy mineral lily cup. The two lily cups were removed from the eavesthrough and placed onto a table. Using a hand magnet inside a glass vile, strongly magnetic minerals such as ulvöspinel were removed from the heavy mineral lily cup and placed into a third lily cup. This hand magnet separation was required to remove the majority of heavy minerals and to prevent any damage to the Frantz magnetic separator. The lily cups were returned to the preparation room and their respective minerals were poured onto a filter paper in a filtration apparatus using ethanol. Once the minerals were sufficiently dry and the filter paper had finished dripping into the flask, the paper was placed onto a hotplate simultaneously under a hot lamp for 20 minutes. While the minerals were drying, the attachments, clamps and spoon were rinsed with water and washed with dish soap. The attachments were sonicated again for 5 minutes and once complete, were returned into the 10% HCl container. Lastly, the dry minerals were removed from the heating setup and slowly poured into a glass vile and labelled. This filtration and drying process was followed for the light minerals, heavy minerals including apatite and biotite and strongly magnetic minerals including ulvöspinel.

The last separation method was based on mineral magnetic susceptibility using a Frantz model L-1 dynamic magnetic separator. Firstly, the elongated stage, vibrator, securing clamps and sample funnel were unscrewed from the Frantz, rinsed with water and sonicated for 5

minutes. During this time, the Frantz was unlocked and rotated to a vertical position to thoroughly clean and wipe the magnets and troughs using ethanol, a spatula and paper towel. Once the sonication was complete, the separator components as well as 2 platinum cups were rinsed with ethanol, dried with compressed air and reinstalled onto the Frantz. The Frantz was rotated 7° frontwards to promote magnetic separation and 4° downwards to promote gravitational and vibrational transport and locked. A small portion of grain separate from the heavy mineral vile was poured into the funnel and the vibrator was turned on. Since the funnel was fully tightened, no grains were permitted to vibrate downwards at first. The current was then turned on to 0.2A in effort to remove any strongly magnetic minerals such as ulvöspinel which remained from the primary hand magnet separation. The funnel was slowly and carefully untightened to allow a narrow stream of mineral grains into the Frantz magnets. The separation was constantly monitored as minerals magnetic at 0.2A were placed into the left cup and nonmagnetic minerals were placed into the right cup. Only on the 0.2A separation was a clean sheet of paper run between the magnets to scrape any strongly magnetic minerals off the magnet to prevent a jam. Once the sample funnel was empty, the current was slowly reduced to 0A and the vibration also reduced to remove any minerals trapped in the middle of the elongated stage. After the 2 cups were filled, the left cup containing the magnetic minerals at 0.2A was emptied onto a clean sheet of paper and returned to its position on the Frantz. The paper was folded and the minerals were poured into a glass vile and labelled. The right cup containing all nonmagnetic minerals at 0.2A was emptied into the sample funnel and also returned to its position. This separation procedure was performed again at 0.6A and 1.6A. The 0.6A run separated slightly magnetic minerals including biotite into the magnetic cup and the 1.6A run separated nonmagnetic minerals including apatite into the nonmagnetic cup. Thus, each sample separation resulted in 4 glass

viles: magnetic at 0.2A, magnetic at 0.6A including biotite, magnetic at 1.6A and nonmagnetic at 1.6A including apatite.

These samples were thoroughly and carefully separated to finally produce enriched apatite and pure biotite grain mounts. Firstly, a polycarbonate mount was drilled with 7 holes and mapped on paper for the sample locations. The mount was also labelled with a diamond etch for the contained mineral. The mount was then rinsed with water and dried with compressed air. Scotch tape was placed on one surface of the mount to secure the grains. Several Kimtech papers were used to cover the workstation, to pour the grains onto and to cover the remaining 6 holes on the mount to prevent contamination while pouring. Regarding the enriched apatite mount, a portion of the nonmagnetic at 1.6A separate was poured onto a folded Kimtech paper and in turn poured into the respective hole in the mount. The pure biotite mount was prepared in a similar fashion although required an additional step. Instead of pouring the magnetic at 0.6A separate directly onto a Kimtech paper, it was poured onto a petri dish covered in ethanol. Using a WILD reflected light microscope, individual biotite grains were isolated and collected using small tweezers and gently placed onto a Kimtech paper. Once the ethanol dried from the paper and the biotite grains were freely moving, they were poured into the respective hole in the mount. Epoxy was prepared once more and carefully poured into each sample hole in the mount. The mount was placed into a vacuum impregnator at 26'' mercury for 5 minutes to minimize any potential air bubbles in the epoxy and remained overnight to harden. Similarly to the thin section procedure, the same cleaning and polishing process was followed using a 45μm diamond pad for 1 minute, 9μm suspended solution and lastly using a 1μm suspended solution each for 5 minutes. The polisher parameters used were 100rpm and 2lbs of pressure pressed on the mount and were purposely conservative to avoid grain plucking.

Electron Microprobe

Mineral compositions were measured using a Cameca SX 50 electron probe microanalyser. Exsolution of ilmenite in ulvöspinel in thin section were individually analysed to determine major and minor oxide concentrations for geothermometry and oxygen fugacity calculations. Additionally, multiple biotite grains in each sample were analysed for major and minor oxides as well as ^{29}Si abundances which was chosen as the standard isotope for the laser ablation data processing. Firstly, the electron microprobe was calibrated and standardized prior to the session. The thin section or grain mount was secured onto a stage, placed in the holder and positioned into the chamber. After manually navigating the sample and having the grain of interest in the centre of the field of view, the point was named and digitized, essentially saving the coordinates into the program memory. Once all the points were located and inputted into the program, the automated analyses began.

Transmitted Light Microscope

Petrographic descriptions of the sample thin sections were done using a Leitz transmitted light microscope and texture images were acquired using a Nikon Coolpix 5400 digital camera. The mineral assemblages, abundances and grain sizes were documented as well as general textures. The equivalent plane polarized and cross polarized images captured groundmass and phenocryst textures, the progressive reaction between amphibole and pyroxene from AP1 to AP7 and apatite paragenesis. The observations were consistently made using a 5X objective lens corresponding to a 4.5mm field of view or a 3mm field of view when using the camera.

Scanning Electron Microscope

Apatite and biotite grain mounts were mapped while ulvöspinel-ilmenite exsolution and apatite-sulphide exsolution textures were imaged using a Jeol JSM-6610LV scanning electron microscope with a 20mm^2 Oxford Instruments SDD for x-rays. Target grains were spotted and their surrounding areas mapped for each sample in both the apatite and biotite mounts to provide assistance in grain location during the laser ablation analyses. The thin section or grain mount was carbon coated, secured onto a stage and attached into the scanning electron microscope chamber which was vented to a 10^{-5} torr vacuum. Sample navigation required the rapid scan rate 2 and imaging was done on the slow, high resolution scan rate 4. The magnification was also increased to 4000X to focus on the grain features and returned to 40X to produce excellent images. Regarding the mapping, apatites were easily distinguishable from silicates by their brighter colour in the backscattered electron image mode whereas the biotites were compositionally confirmed using point analyses with the corresponding INCA software spectra. Moreover, zoning in apatite was searched for using cathode luminescence imaging without success. Specific equipment settings include a voltage of 15KeV, a 30 second count time, a 28,000 counts/sec rate and a 1µA sample current.

Laser Ablation Inductively Coupled Plasma Mass Spectrometer

The trace element concentrations of several minerals were determined using a UP 213 laser ablation system and the VG PQ ExCell inductively coupled plasma mass spectrometer. The first session required measuring the low abundances of Li, Zn, Cu, Sn, Rb, Cs, Pb, Bi, Mo, REEs, Sr, Th and U in apatites and biotites in each sample as proposed by Johnson and Canil (2011), MacKenzie and Canil (2011) and Rubin (1997). The following analyses specifically

focused on measuring the most volatile trace elements, Li, Rb, Pb and Bi, in biotite, pyroxene, plagioclase and amphibole in AP3, representing a cumulate rock, and in AP7, resembling a quenched liquid. ^{43}Ca was chosen as the standard isotope for apatite analyses and ^{29}Si was selected as the standard isotope for the remaining minerals. The thin section or grain mount was firstly polished in 0.3µm silica powder, sonicated in hexane for 10 minutes to remove any carbon coating and dried with ethanol. Then the sample was levelled onto a stage and positioned under the laser apparatus. Specific instrument parameters include a constant zoom view of 25%, a laser power output of 45%, a 10Hz rep rate and a 40µm/s scan speed. The nebulizer gas flow was set at 0.58L/min and the oxide values were acceptable at $\frac{^{248}\mathrm{ThO}}{^{232}\mathrm{Th}} = 0.001$ and $\frac{^{238}\mathrm{U}}{^{232}\mathrm{Th}} = 1.03$. The target minerals in the thin section or grain mount were then identified and trench lines or spots were digitally inputted into the program. Once all the laser sites were chosen, two NIST 610 glass standards were analysed prior to and another two after the suite of individual grains. The laser spot size was varied from 20-55µm depending on the specific mineral dimensions. Lastly, the software-generated tables containing the trace element concentrations were transferred over to the adjacent computer. The Glitter data processing first required inputting the standard isotope concentration determined from the electron microprobe or from the online database Webmineral and then manually adjusting the background and signal intervals before the correct element concentrations were recalculated and provided.

Results

Sample Mineral Abundances and Textures

The collected hand samples are exhibited in Figure 4.1; their mineral modal abundances are presented in Table 4.1 and their variation trends are given visually in Figure 4.2. Figure 4.3 demonstrates the progressive reaction between amphibole and pyroxene as well as apatite paragenesis as an early phase while general textures are shown in Figure 4.4. AP1 has an overall porphyritic texture with feldspar, nepheline (0.5-5mm) and amphibole (0.5-3mm) phenocrysts. Amphibole appears stable. AP2 has large feldspar phenocrysts (0.2-1cm) and relatively large apatite (50-500µm) crystals as inclusions in every mineral phase. Amphibole (0.25-5mm) and oxides (50µm-1mm) surround pyroxene (1-4mm) crystals (Figure 4.3C). AP3 has a distinctive porphyritic cumulate texture (Figure 4.4A) and is compositionally layered with feldspar (0.5-5mm) and biotite (0.5-3mm) crystals oriented $\pm 40^{\circ}$ with respect to each other (Figure 4.4B). Pyroxene (0.5-4mm) crystals are more prominent and once more occur with amphibole (0.5-5mm) along their rims. AP4 also has an overall porphyritic and phaneritic texture with feldspar (0.5-5mm) and pyroxene (0.5-5mm) phenocrysts. The feldspar and biotite crystals no longer appear oriented with respect to each other. Pyroxene is altered to amphibole (0.5-2mm). AP5 is more aphanitic although includes large pyroxene (0.1-5mm) as well as feldspar and nepheline (0.2-1cm) phenocrysts. Amphibole (0.1-2mm) is consistently surrounding pyroxene crystals. Pyroxene is also zoned with many apatite (50-400µm) and oxide (50µm-1mm) inclusions. AP6 is similarly aphanitic in texture. Amphibole (0.1-2mm) crystals are less prominent while pyroxene (0.2-3mm) occurs as distinct phenocrysts. Feldspar (0.1-2mm) is characterized by smaller crystal sizes and phenocrysts are now absence. Lastly, AP7 has a distinctive aphanitic groundmass texture and resembles a quenched liquid (Figure 4.4C). Amphibole (0.1-1mm) is

scarce while pyroxene (0.1-5mm) crystals are more abundant as given in Figure 4.2. This figure illustrates how amphibole (green) progressively decreases in abundance as pyroxene (light blue) consequently increases in abundance from the margin to the core of the intrusion. There are several examples of 5mm pyroxene phenocrysts riddled with apatite (50-800µm) inclusions and unstable amphibole crystals.

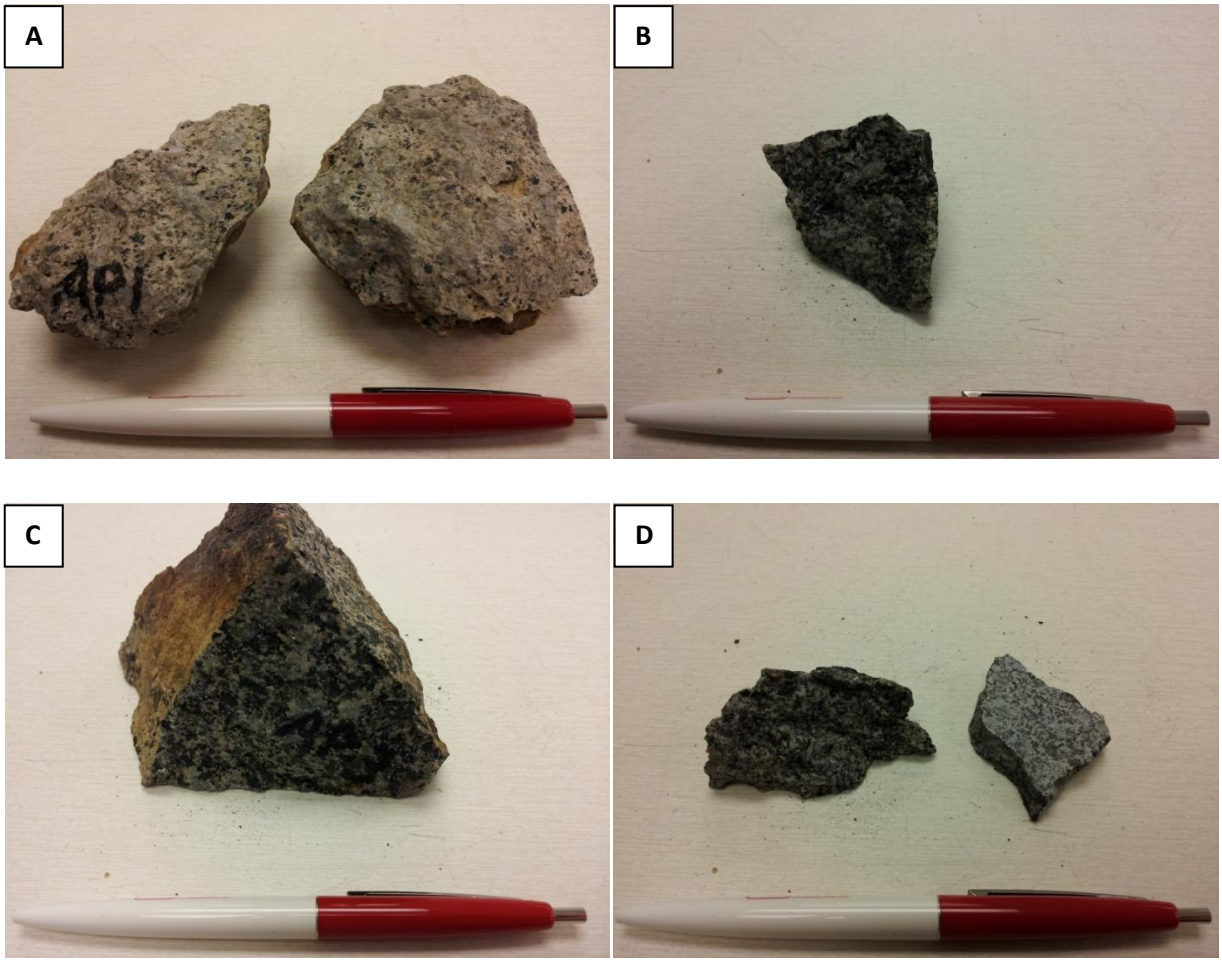

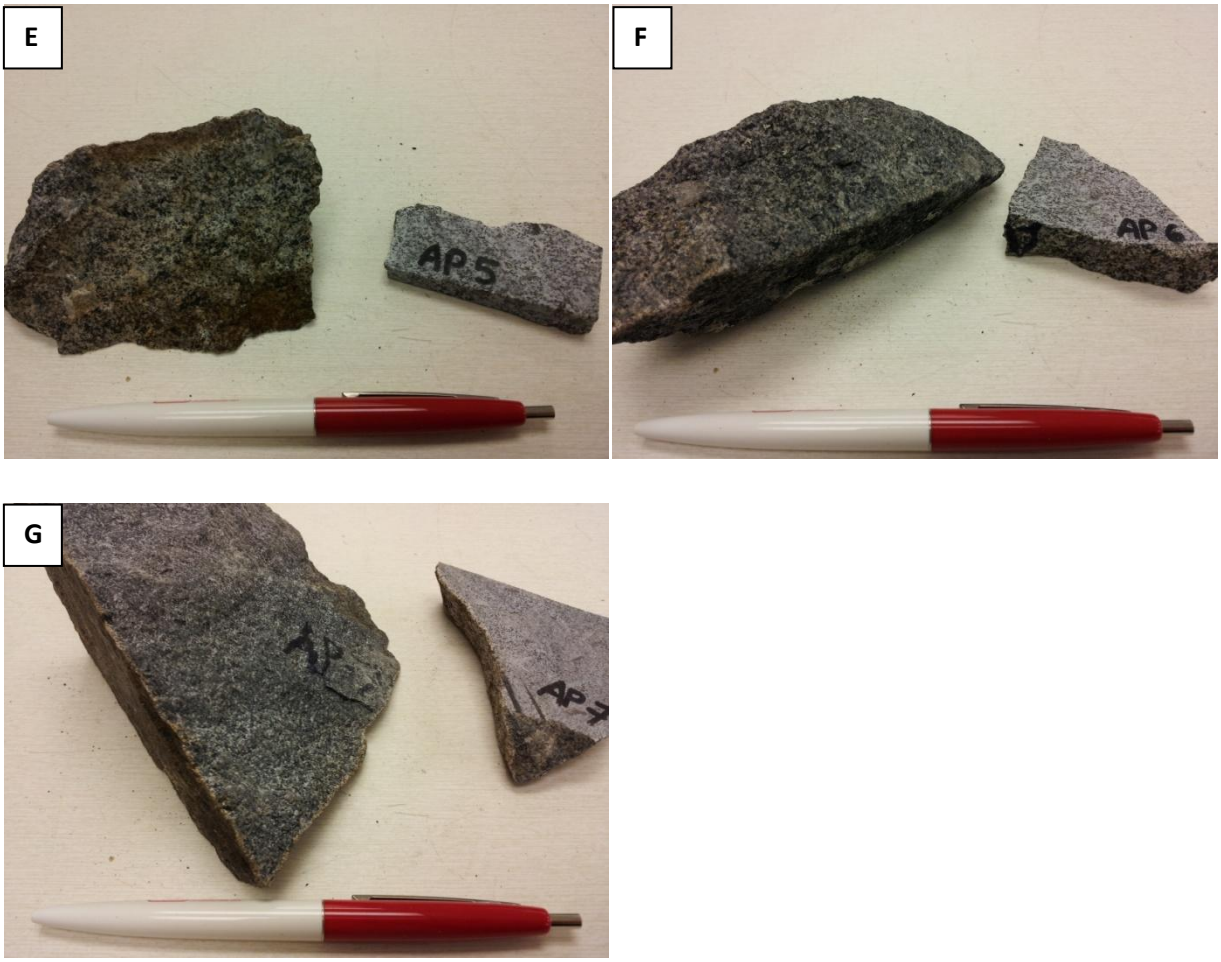

Figure 4.1: Digital camera images of hand samples at the Mt. St. Grégoire intrusion. A: AP1. B: AP2. C: AP3. D: AP4. E: AP5. F: AP6. G: AP7.

Table 4.1: Sample mineral modal abundances (%) at the Mt. St. Grégoire intrusion

	Feldspar	**Nepheline**	**Amphibole**	**Biotite**	**Pyroxene**	**Oxide**	**Apatite**
AP1	75	10	7	2	2	2	2
AP2	56	6	15	5	10	5	3
AP3	65	5	10	8	5	5	2
AP4	65	0	5	5	15	8	2
AP5	55	15	10	3	10	5	2
AP6	75	0	2	3	10	8	2
AP7	70	5	2	1	12	8	2

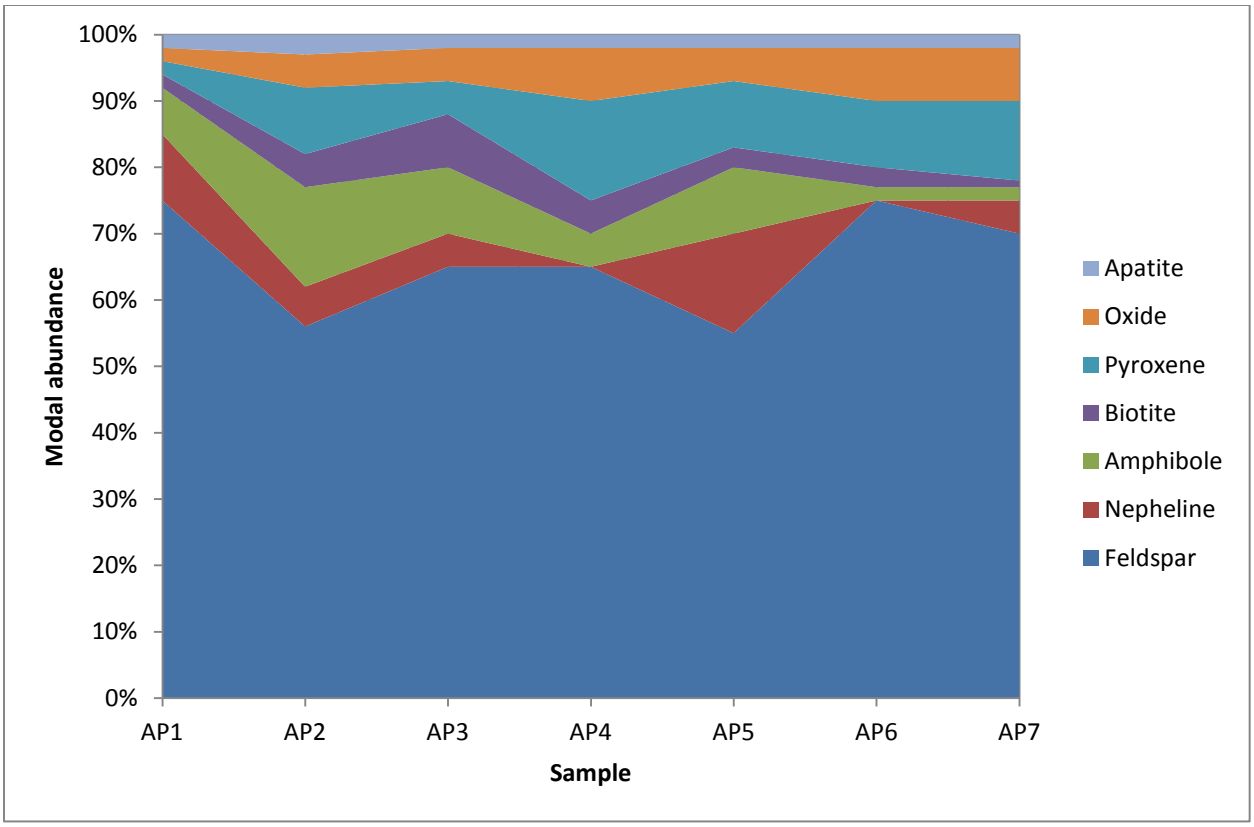

Figure 4.2: Graphical representation of the variation in sample mineral abundances at the Mt. St. Grégoire intrusion.

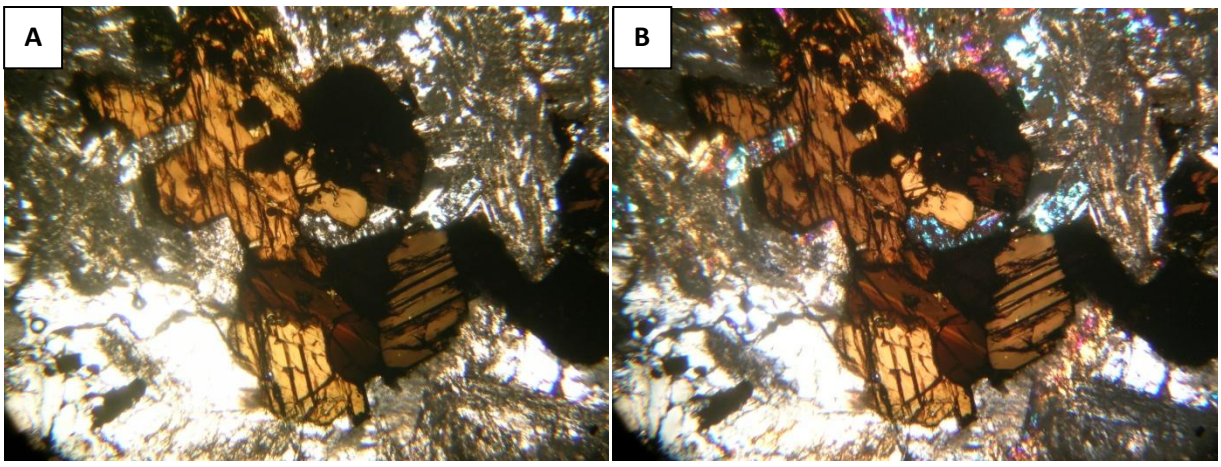

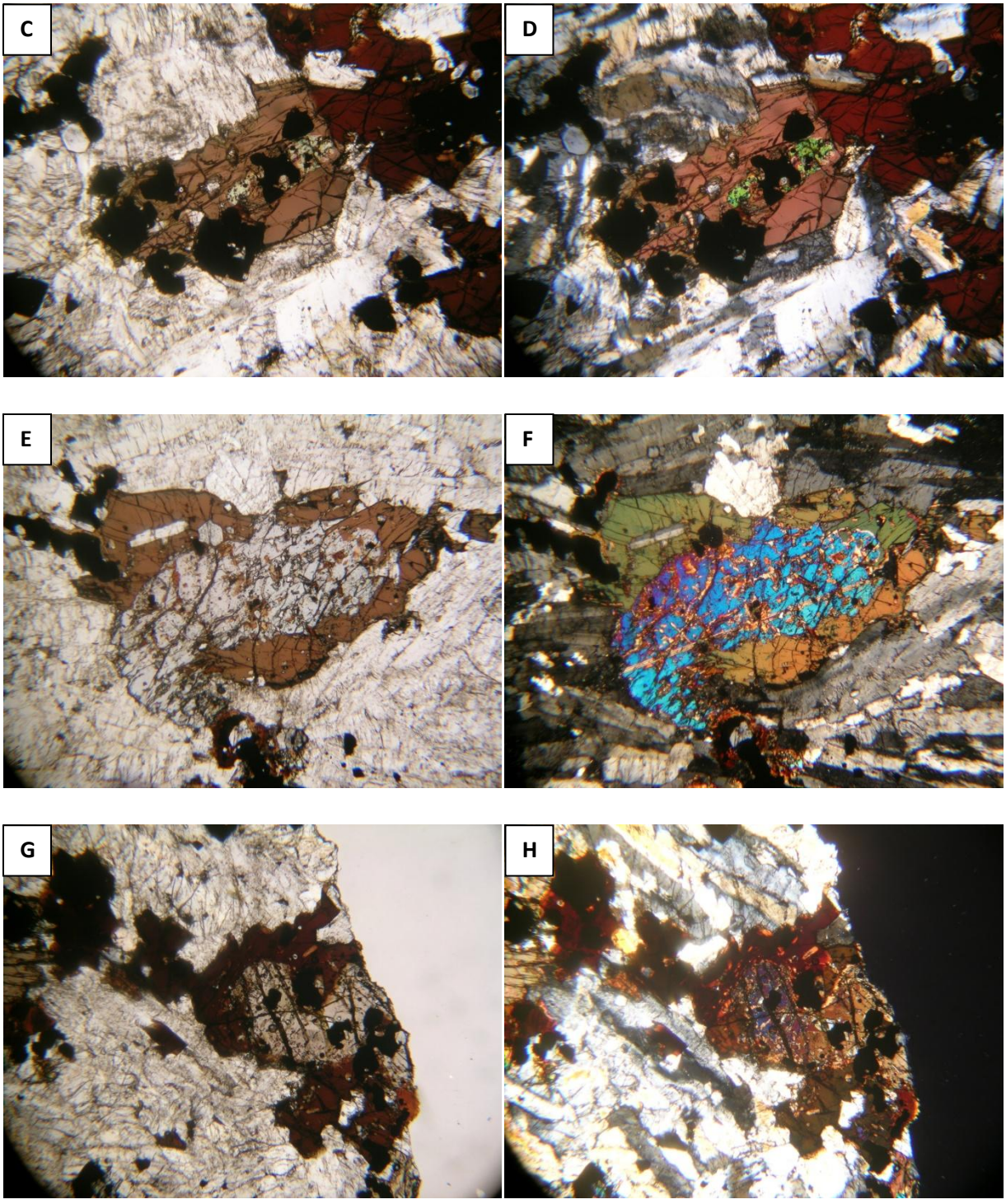
C
D
E
F
G
H

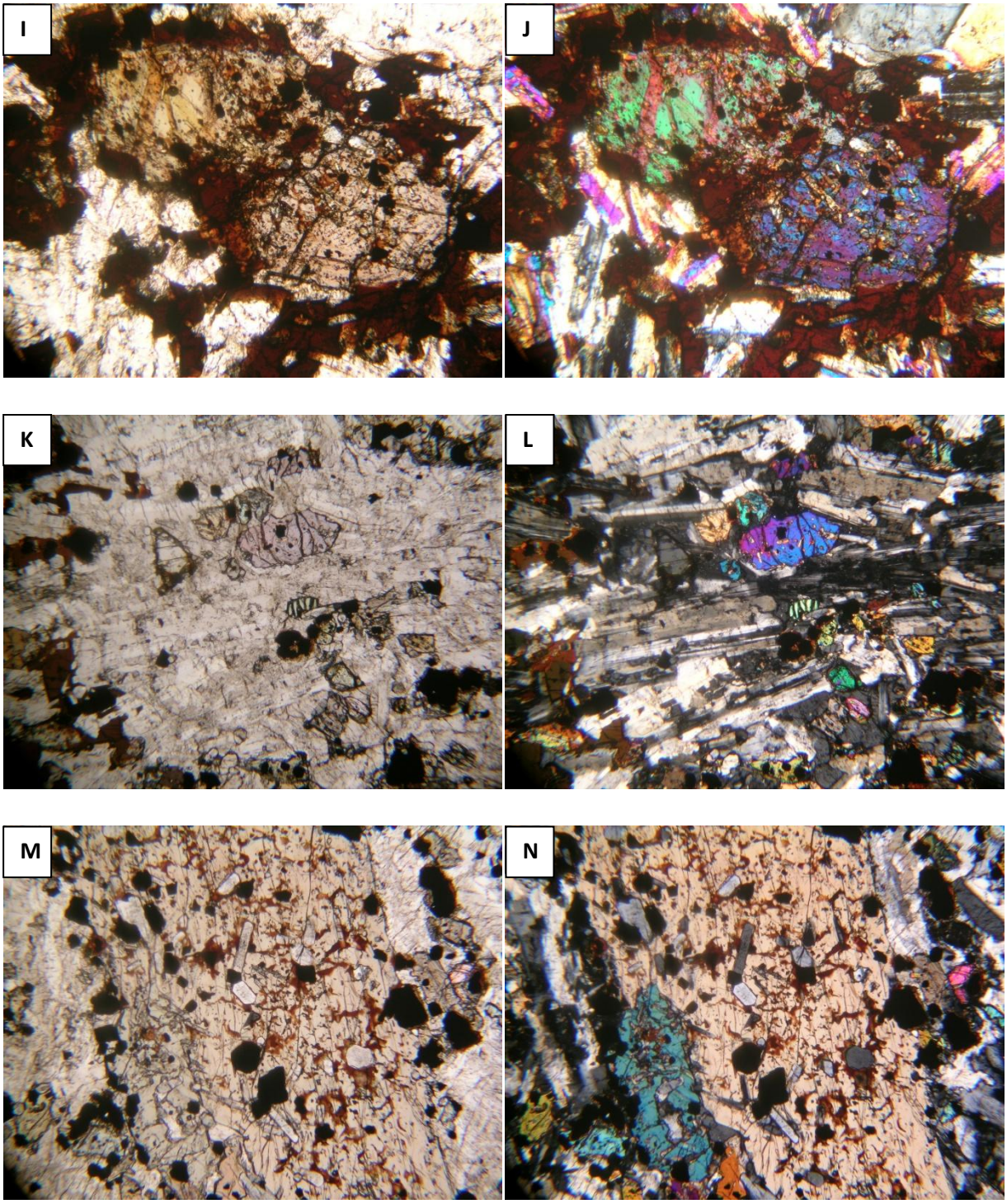

Figure 4.3: Plane polarized light (left) and cross polarized light (right) images of samples at the Mt. St. Grégoire intrusion. Apatite is an early phase and occurs as inclusions in every mineral phase in all samples. Field of view is 3mm. A, B: AP1, amphibole stable, pyroxene nearly

absent. C, D: AP2, large amphibole rim surrounding small pyroxene core. E, F: AP3, amphibole rim surrounding pyroxene core. G, H: AP4, amphibole rim surrounding pyroxene core. I, J: AP5, small amphibole rim surrounding large pyroxene core. K, L: AP6, pyroxene stable, amphibole nearly absent. M, N: AP7, pyroxene stable, amphibole nearly absent.

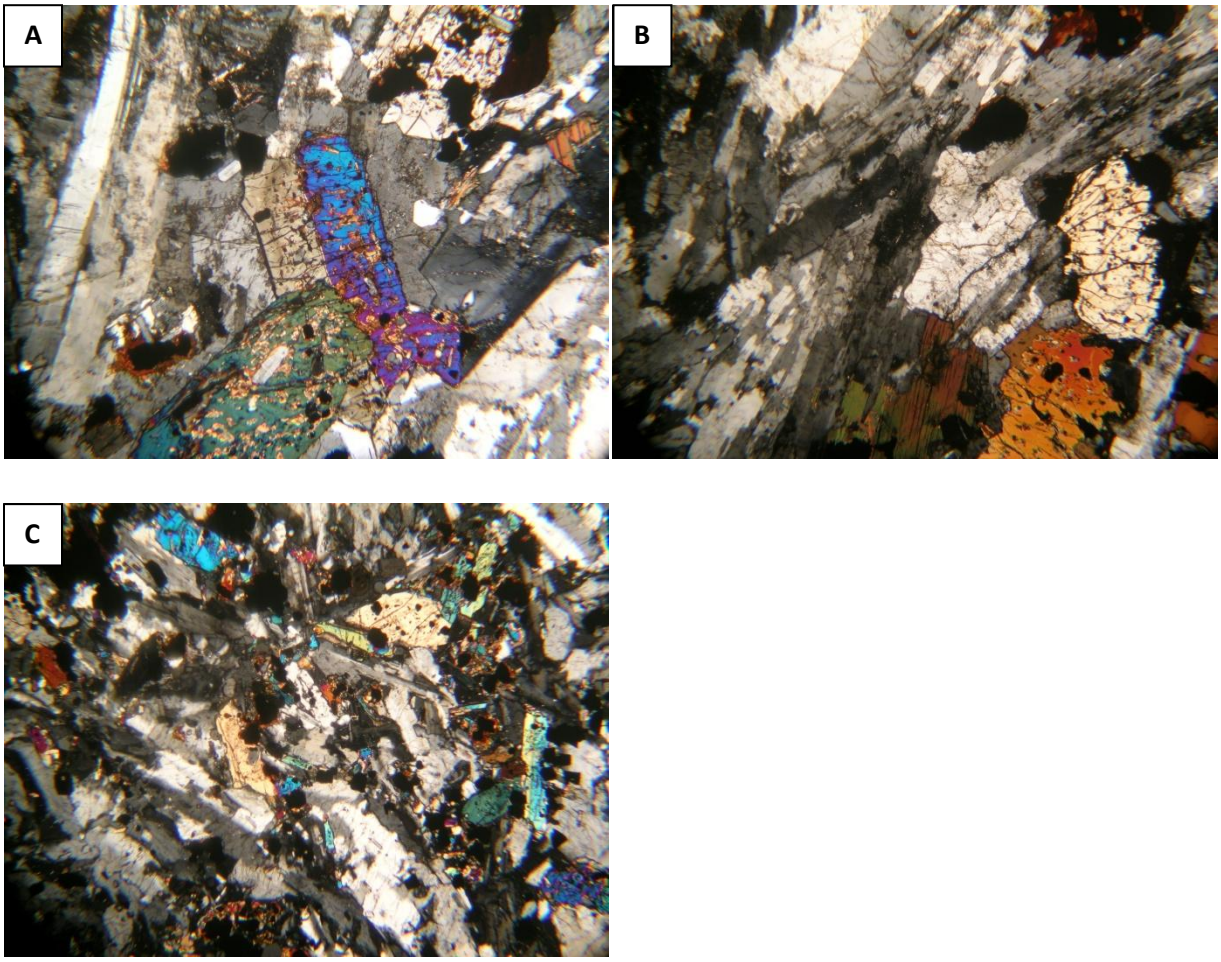

Figure 4.4: Cross polarized light images of samples at the Mt. St. Grégoire intrusion. Field of view is 3mm. A: AP3, porphyritic cumulate texture. B: AP3, compositional layering from preferential orientation of feldspar and biotite crystals. C: AP7, quenched liquid texture.

Apatite Textures

Figure 4.5 illustrates 1µm-sized sulphide exsolution in apatite grains from multiple samples. These consist of FeS and occur in various orientations; Figure 4.5A shows the exsolution in the horizontal plane appearing rod-like while Figure 4.5B shows the exsolution in the vertical axis appearing point-like. Regarding distribution, the exsolution is principally concentrated in the centre of apatite crystals rather than along the rim and is easily visible under 10X magnification causing the apatite to have a dusty appearance Furthermore, FeTiO-composed inclusions were observed in some apatite grains as given in Figure 4.6.

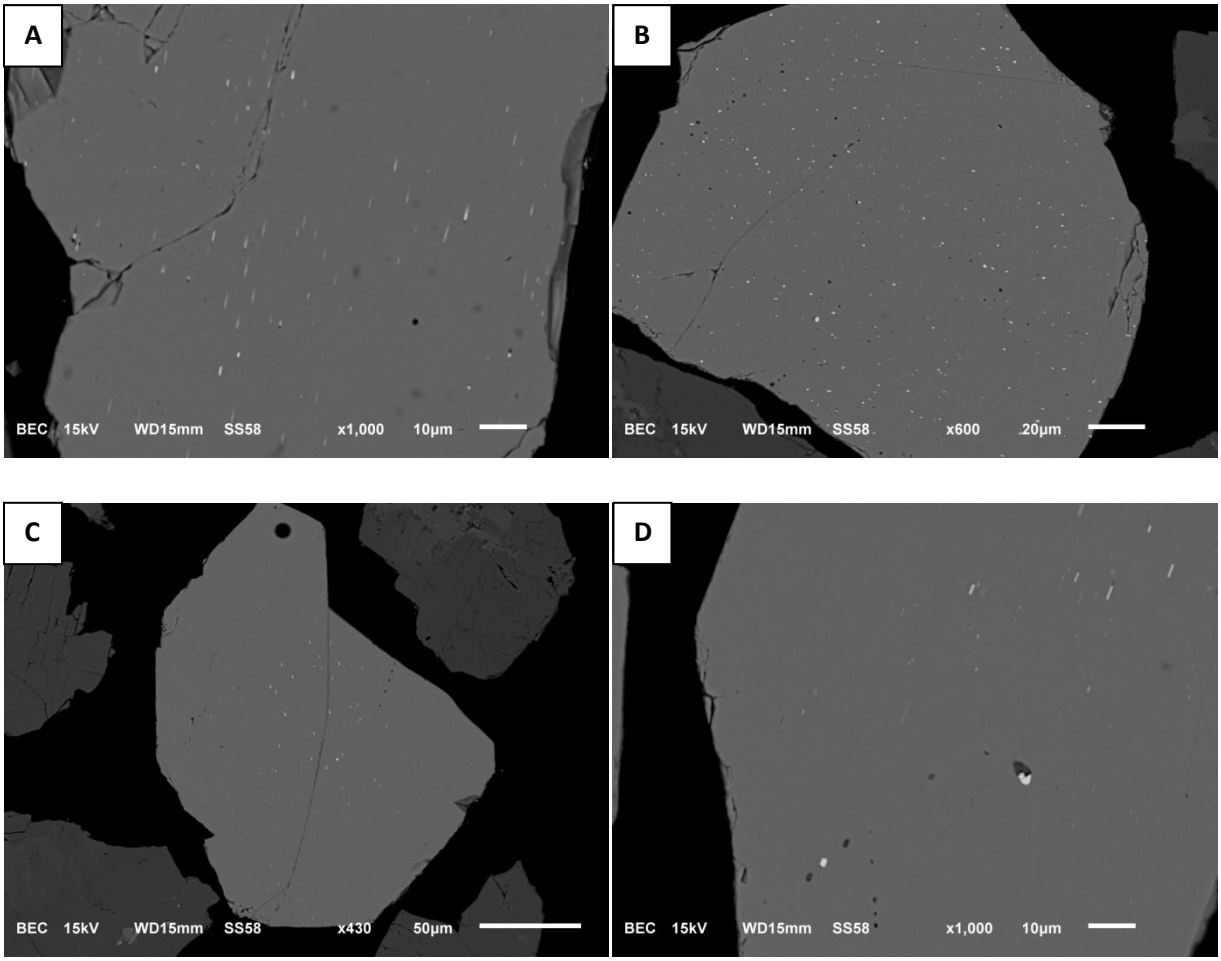

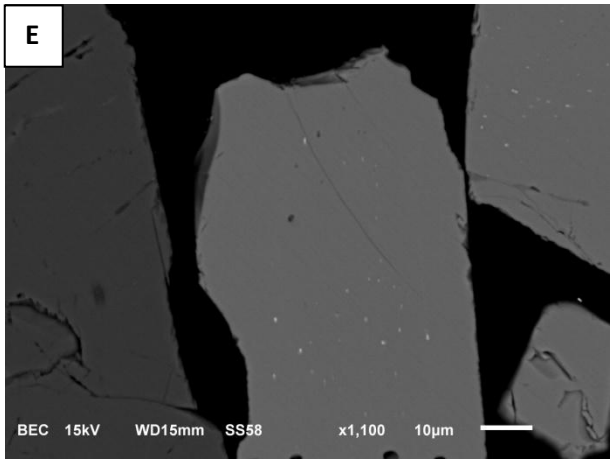

Figure 4.5: Apatite-sulphide exsolution scanning electron microscope images of samples at the Mt. St. Grégoire intrusion. A: AP2. B: AP3. C: AP5. D: AP6. E: AP7.

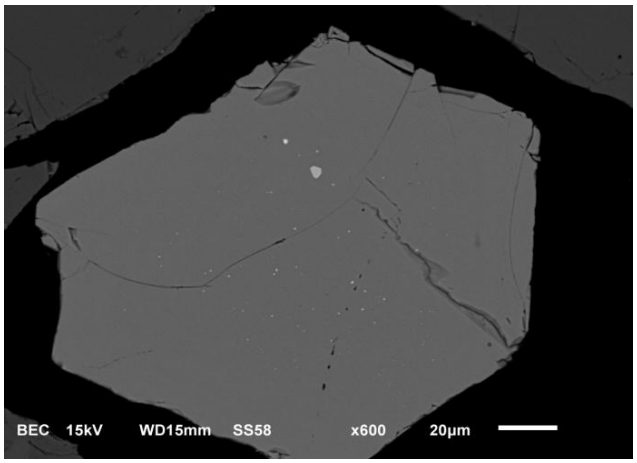

Figure 4.6: Apatite-oxide inclusions scanning electron microscope image of sample AP4 at the Mt. St. Grégoire intrusion.

Sample Geothermobarometry

Table 4.2 and Table 4.3 display the average oxide concentrations in ulvöspinel and in ilmenite, respectively. These data were sorted to only include <0.10% SiO_2, 97-102% oxide totals and overall expected FeO and TiO_2 values for their respective mineral with low standard deviations for all oxide concentrations. The compositional analyses were limited to single oxide grains of ulvöspinel with ilmenite exsolution as demonstrated in Figure 4.7.

Table 4.2: Average oxide concentrations (wt%) in ulvöspinel at the Mt. St. Grégoire intrusion

	Al_2O_3	**SiO_2**	**MnO**	**FeO**	**CaO**	**TiO_2**	**Cr_2O_3**	**MgO**	**Oxide totals**
AP2	1.55	0.05	1.61	81.37	0.01	12.71	0.026	0.26	97.59
AP3	1.97	0.02	1.74	81.14	0.03	12.59	0.02	0.42	97.93
AP4	2.36	0.04	1.74	72.96	0.01	19.6	0.01	1.02	97.76
AP5	1.9	0.04	1.77	73.11	0.03	19.99	0.02	0.98	97.84
AP6	2.35	0.05	1.56	72.53	0.02	20.46	0.01	1.23	98.19
AP7	2.64	0.05	1.67	73.37	0.01	19.68	0.01	1.53	98.94

Table 4.3: Average oxide concentrations (wt%) in ilmenite at the Mt. St. Grégoire intrusion

	Al_2O_3	**SiO_2**	**MnO**	**FeO**	**CaO**	**TiO_2**	**Cr_2O_3**	**MgO**	**Oxide totals**
AP2	0.00	0.01	3.43	44.73	0.05	50.73	0.01	1.37	100.3
AP3	0.02	0.02	3.55	44.92	0.03	50.06	0.02	1.28	99.9
AP4	0.01	0.02	2.37	43.84	0.01	50.79	0.01	2.14	99.2
AP5	0.01	0.05	3.03	45	0.04	50.07	0.01	1.2	99.4
AP6	0.03	0.02	1.96	43.87	0.07	50.6	0.01	2.54	99.1
AP7	0.14	0.02	2.18	44.56	0.02	49.74	0.01	2.76	99.43

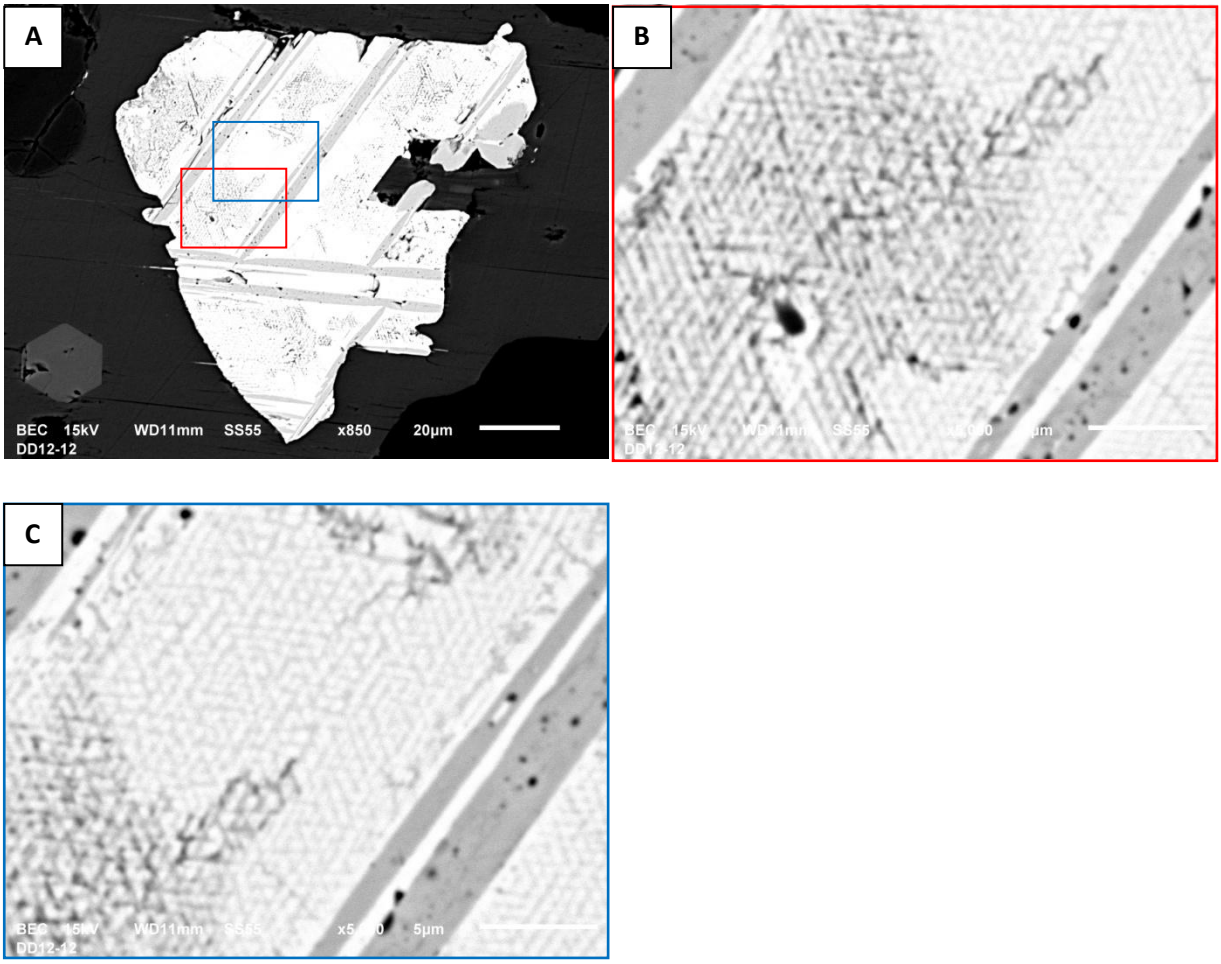

Figure 4.7: Ulvöspinel-ilmenite exsolution (lighter-darker, respectively) scanning electron microscope image of sample AP5 at the Mt. St. Grégoire intrusion. A: 850X magnification. B, C: 5000X magnification of colour-outlined zones.

Ghiorso and Evans (2008) released an online Fe-Ti oxide geothermometry and oxygen fugacity calculator based on their constitutive oxides and assuming a crystallization pressure of 200MPa. The Fe-Ti exchange temperatures and oxygen fugacity conditions relative to nickel-nickel oxide (NNO), provided in Table 4.4, were calculated using their computation thermodynamic model and the oxide concentrations in Tables 4.2 and 4.3. Thus, all the samples were measured to be reduced relative to NNO and range in ΔNNO from -1.41 to -2.04. Note, AP1 was excluded from this analysis due to the exsolution being inconsistent and poorly defined

throughout the thin section. The oxide thermometry and oxygen fugacity values were determined using these reactions, respectively:

$Fe_2O_3 + Fe_2TiO_4 \leftrightarrow Fe_3O_4 + FeTiO_3$ (1)

$2\ Fe_2O_3 + 6\ FeTiO_3 \leftrightarrow 6\ Fe_2TiO_4 + O_2$ (2)

where the first reaction is temperature-dependent and the second reaction is oxygen fugacity-dependent. The uncertainty in the exchange temperatures varies from 50 to 100°C due to analytical error whereas oxygen fugacity estimates are fairly accurate and insensitive to analytical uncertainty, Ghiorso and Evans (2008).

Table 4.4: Fe-Ti oxide geothermometry and oxygen fugacity values, calculated from Ghiorso and Evans (2008)

	Fe-Ti exchange T (°C)	**$Log_{10}fO_2$ (ΔNNO)**
AP2	702	-1.77
AP3	731	-1.41
AP4	790	-2.04
AP5	812	-1.67
AP6	830	-1.78
AP7	798	-1.9

Biotite Major and Minor Oxide Concentrations

The average oxide concentrations in biotite are given in Table 4.5. These data were sorted to only include 97-102% oxide totals and overall expected F, Cl and FeO values with low standard deviations for all oxide concentrations. Additionally, the concentration trends for F, Cl, FeO and MgO in each sample along the intrusion are demonstrated in Figure 4.8. F (blue), Cl (red) and MgO (purple) progressively decrease in abundance while FeO (green) significantly increases in abundance from the core to the margin of the intrusion.

Table 4.5: Average oxide concentrations (wt%) in biotite at the Mt. St. Grégoire intrusion

	AP1	**AP2**	**AP3**	**AP4**	**AP5**	**AP6**	**AP7**
F	0.88	0.46	0.65	0.99	0.84	0.82	1
Na_2O	0.49	0.49	0.53	0.51	0.43	0.35	0.56
MgO	7.53	9.02	10.86	12.33	12.55	12.29	13.09
Al_2O_3	12.21	12.78	13.08	12.75	13.08	13.25	12.93
TiO_2	5.73	6.24	8.32	8.54	8.05	7.76	8.85
MnO	1.44	1	0.41	0.31	0.31	0.32	0.21
FeO	26.04	23.02	19.81	16.81	16.99	17.73	15.44
K_2O	8.61	8.92	9.12	9.15	9.33	9.32	9.16
SiO_2	36.02	36.78	36.73	37.22	36.93	36.89	36.87
Cl	0.049	0.039	0.035	0.054	0.053	0.052	0.074
CaO	0.14	0.06	0.03	0.05	0.05	0.08	0.04
Oxide totals	98.79	98.68	99.49	98.38	98.4	98.96	97.93

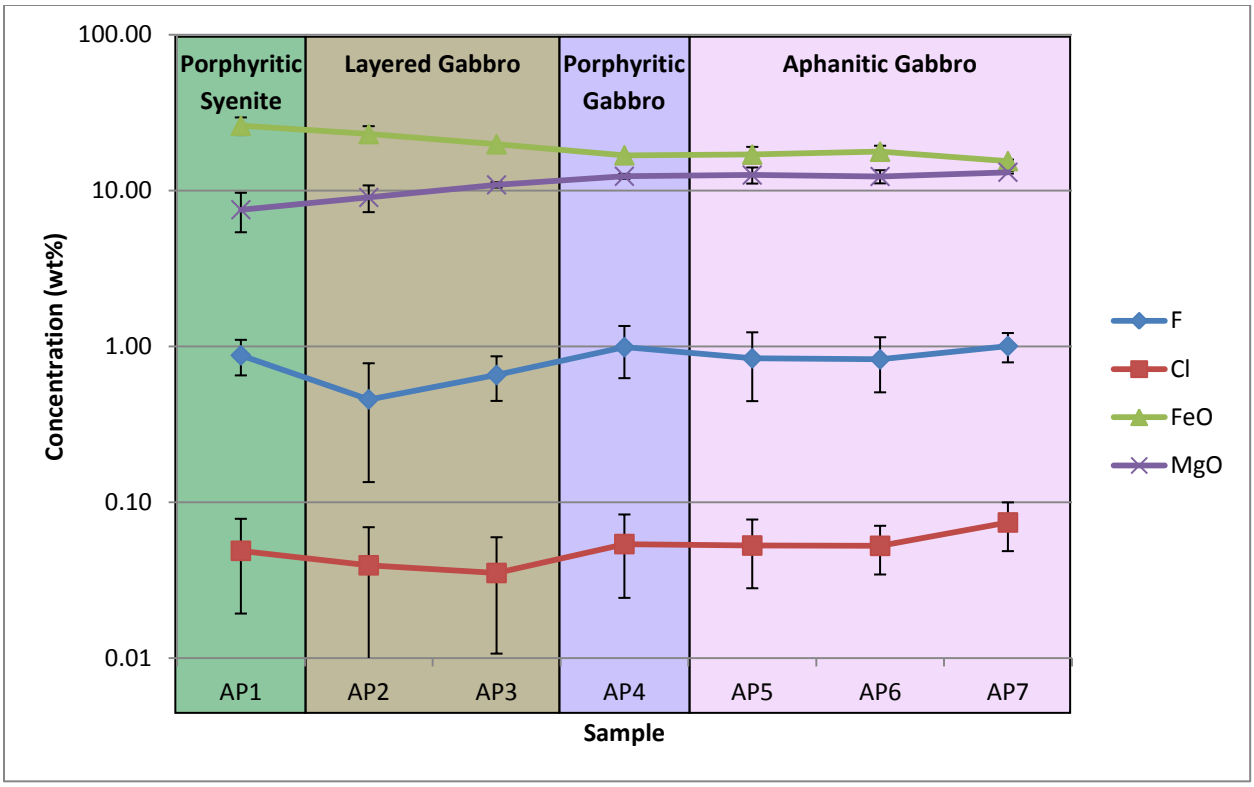

Figure 4.8: Graphical representation of the concentration trends (log-scale) for F, Cl, FeO and MgO in biotite at the Mt. St. Grégoire intrusion with 1σ error bars.

Sample Trace Element Concentrations

The average trace element concentrations in apatite and biotite are listed in Table 4.6 and Table 4.7, respectively. The data was sorted to only include overall expected element values for apatite with low standard deviations for all concentrations since only a single set of biotite analyses were obtained.

Table 4.6: Average trace element concentrations (ppm) in apatite at the Mt. St. Grégoire intrusion

	AP1	**AP2**	**AP3**	**AP4**	**AP5**	**AP6**	**AP7**
Li7	0.61	0.49	0.47	0.51	0.46	0.42	0.45

Si29	5582	32412	1071	1356	1354	1584	1361
Ca43	393585	393585	393585	393585	393585	393585	393585
Fe57	1085.16	2832.24	1375.41	3507.48	1575.02	2339.35	1807.29
Cu65	1.21	9.10	2.70	9.99	1.94	5.21	4.33
Zn66	1.56	2.80	0.48	2.57	1.39	1.13	1.45
Rb85	1.28	0.64	0.25	0.60	0.16	0.22	0.31
Sr88	1793.37	3851.65	2901.77	2535.15	3164.91	3043.92	2777.99
Mo95	0.18	0.44	0.39	1.36	0.20	0.20	0.27
Sn118	0.20	0.19	0.16	0.27	0.19	0.21	0.18
Cs133	0.07	0.08	0.07	0.07	0.07	0.07	0.07
La139	5646.28	1878.64	1817.45	2171.91	1983.53	2209.08	2267.15
Ce140	11644.32	4080.05	3871.83	4452.01	4221.99	4704.02	4803.50
Pr141	1067.18	310.78	291.63	338.79	345.93	391.89	368.77
Nd146	4453.00	1378.22	1324.98	1496.80	1530.79	1637.77	1642.52
Sm147	543.98	228.53	220.57	251.79	258.96	275.24	276.68
Eu153	111.89	59.52	56.54	59.63	62.86	65.71	64.33
Gd157	361.54	159.53	157.95	177.65	185.18	194.65	195.03
Tb159	41.25	18.62	18.05	20.29	22.17	24.01	22.46
Dy163	227.10	94.22	91.71	109.08	108.67	117.21	118.06
Ho165	34.71	15.16	14.66	16.91	17.93	19.84	18.50
Er166	87.54	35.11	34.32	42.11	40.01	44.01	44.51
Tm169	9.12	3.89	3.71	4.62	4.41	5.06	4.79
Yb172	54.31	22.40	21.91	28.63	24.70	28.03	28.77
Lu175	6.45	2.69	2.66	3.57	3.03	3.46	3.48
Pb208	2.26	3.01	2.39	4.04	1.53	2.19	2.42
Bi209	0.04	0.03	0.02	0.04	0.02	0.02	0.03
Th232	54.21	17.82	15.89	32.58	25.25	23.25	28.00
U238	9.60	3.72	3.69	7.40	5.76	5.29	6.57

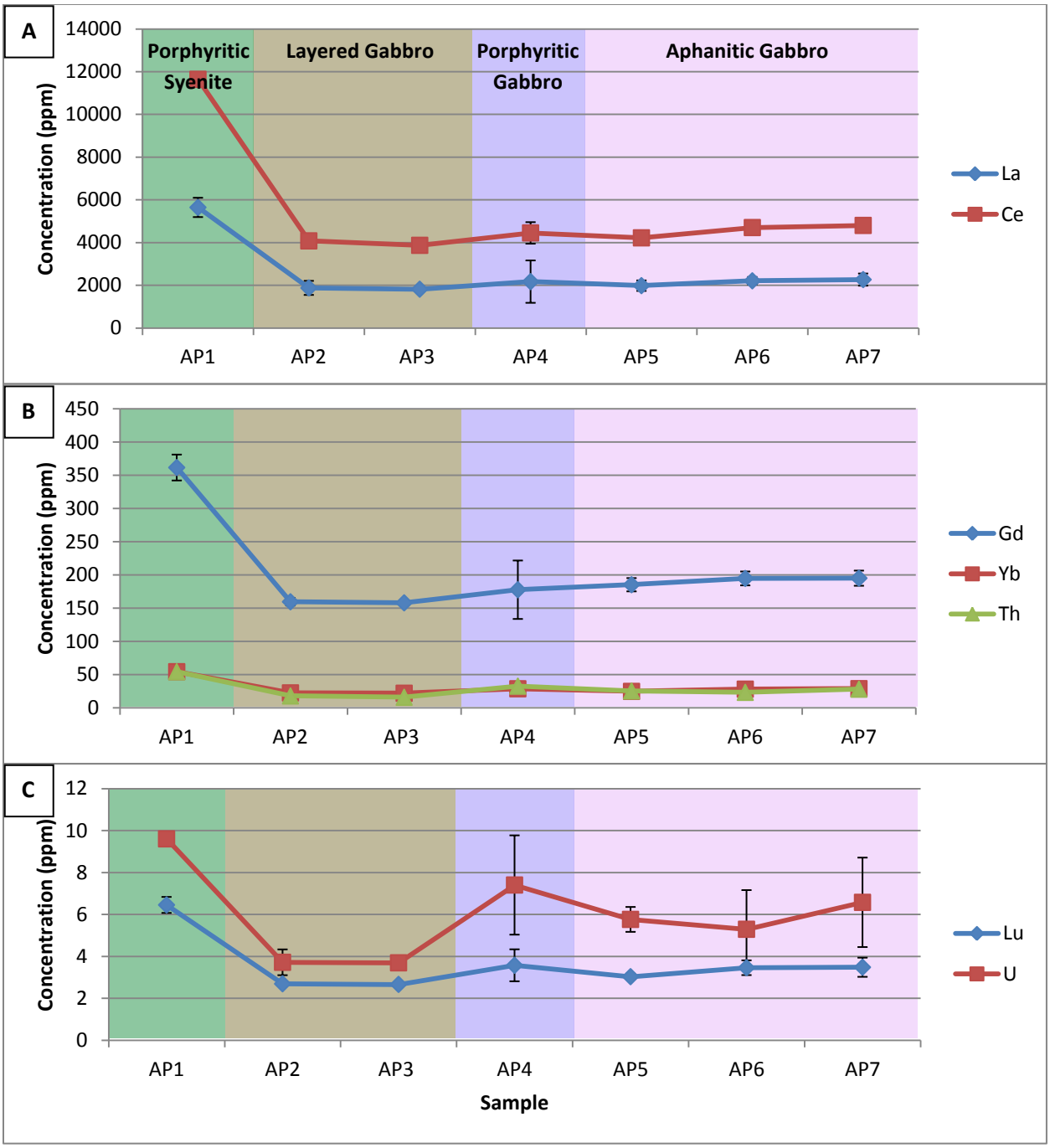

Figure 4.9: Graphical representation of the concentration trends for trace elements in apatite at the Mt. St. Grégoire intrusion with 1σ error bars. A: Variation in La and Ce. B: Variation in Gd, Yb and Th. C: Variation in Lu and U.

The REEs, Th and U concentrations in apatite are shown in Figure 4.9. Generally, these concentrations decrease in abundance from the core to the margin of the intrusion. The exception is sample AP1, the porphyritic syenite unit, as the most enriched in each of the above trace elements. Additionally, AP4 appears somewhat anomalous, especially in the low concentrations such as with U, where it has a higher concentration than AP5, AP6 and AP7. However, this may also be ignored due to the large error involved.

Biotite trace element concentrations were initially corrected for apatite inclusion contamination using the equations:

$$\chi_{bio} = \frac{C_{tot}^{La} - C_{ap}^{La}}{C_{bio}^{La} - C_{ap}^{La}} \qquad (3)$$

$$C_{bio} = \frac{C_{tot} - (C_{ap}\chi_{ap})}{\chi_{bio}} \qquad (4)$$

where χ_{bio} is the biotite mass fraction, χ_{ap} is the apatite mass fraction, C_{tot}^{La} is the measured La concentration from the biotite analysis, C_{ap}^{La} is the measured La concentration from the apatite analysis and C_{bio}^{La} is the corrected La concentration for apatite-free pure biotite.

Table 4.7: Average trace element concentrations (ppm) in biotite at the Mt. St. Grégoire intrusion

	AP1	**AP2**	**AP3**	**AP4**	**AP5**	**AP6**	**AP7**
Li7	380.53	5.91	70.04	70.28	23.08	22.63	35.93
Si29	168302	168168	171608	173966	172635	172959	173755
Ca43	330.08	122973	89.12	440.15	2729.63	211.52	554.06
Fe57	333004	46143	189440	186498	102894	128670	141793
Cu65	12.57	18.02	2.06	2.82	2.79	13.71	29.17
Zn66	1593.67	27.79	328.89	200.01	120.76	154.26	183.63
Rb85	715.87	37.33	625.73	870.67	425.57	445.98	538.10

Sr88	13.37	113.51	68.13	121.91	96.52	70.57	122.98
Mo95	1.18	0.82	1.41	2.29	1.37	1.84	1.67
Sn118	1.00	2.92	2.45	2.12	1.52	2.26	2.06
Cs133	2.61	1.35	2.92	4.31	2.91	2.84	1.95
La139	0.05	0.05	0.06	0.06	0.05	0.05	0.05
Ce140	0.00	19.87	0.04	0.26	0.12	0.00	0.00
Pr141	0.00	7.88	0.01	0.04	0.16	0.07	0.12
Nd146	0.00	46.41	0.04	0.31	0.91	0.15	0.18
Sm147	0.00	12.47	0.06	0.04	0.33	0.15	0.00
Eu153	0.00	3.67	0.04	0.19	0.20	0.09	0.13
Gd157	0.00	10.18	0.09	0.08	0.24	0.07	0.08
Tb159	0.00	1.45	0.01	0.01	0.04	0.01	0.01
Dy163	0.00	8.65	0.02	0.02	0.24	0.02	0.13
Ho165	0.01	1.56	0.01	0.01	0.03	0.00	0.00
Er166	0.01	3.87	0.01	0.02	0.11	0.03	0.03
Tm169	0.02	0.45	0.01	0.01	0.01	0.01	0.01
Yb172	0.07	3.40	0.03	0.07	0.09	0.06	0.08
Lu175	0.03	0.42	0.01	0.02	0.02	0.01	0.02
Pb208	0.69	1.14	0.97	1.30	1.05	0.85	2.21
Bi209	0.04	0.09	0.01	0.02	0.02	0.03	0.02
Th232	0.00	0.27	0.09	0.12	0.58	0.26	0.14
U238	0.02	0.03	0.03	0.11	0.27	0.06	0.18

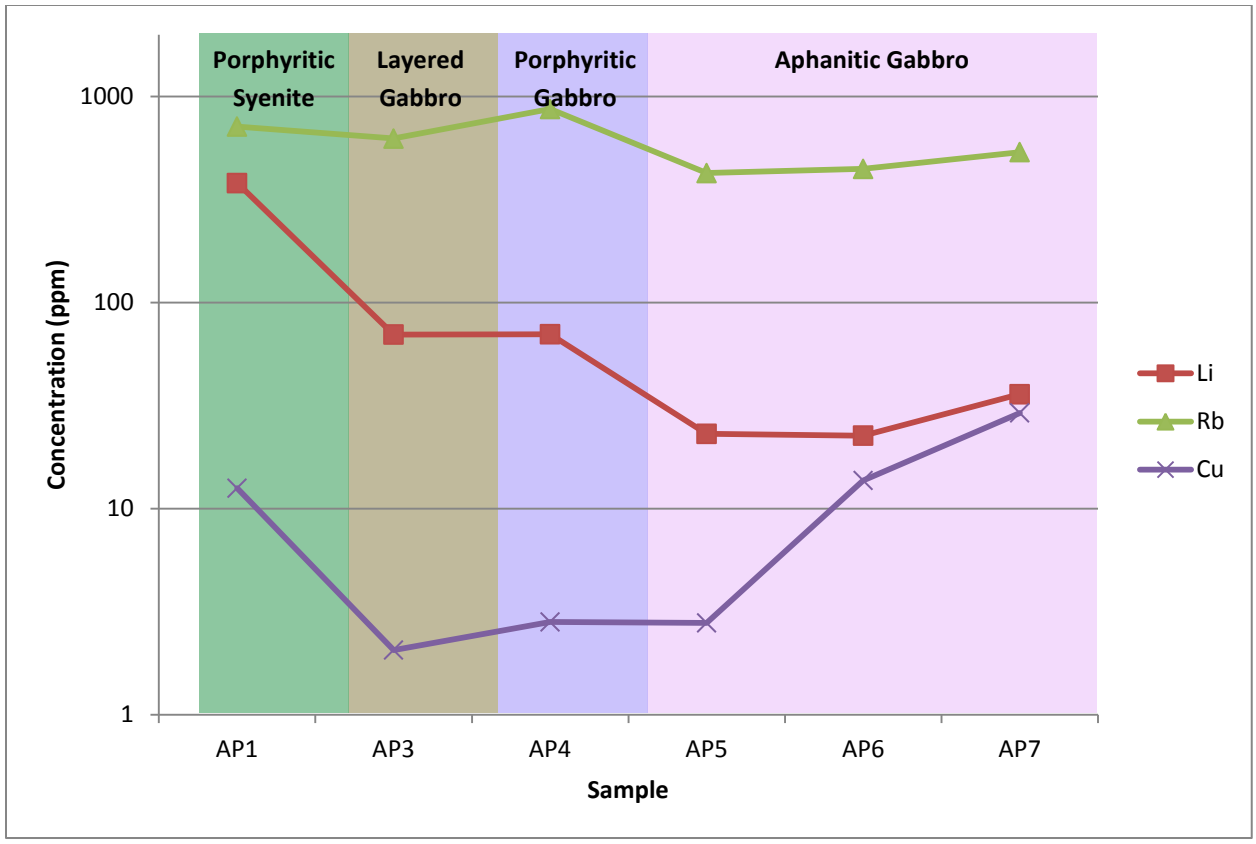

Figure 4.10: Graphical representation of the concentration trends (log-scale) for trace elements in biotite at the Mt. St. Grégoire intrusion with no available error bars.

The concentrations for Li, Rb and Cu in biotite are demonstrated in Figure 4.10. Rb (green) and Li (red) progressively increase in abundance from the core to the margin of the intrusion. In contrast, Cu (purple) significantly decreases in abundance although is once more enriched in sample AP1. Note, AP2 was excluded from this figure due to its unusual measured concentrations; high Ca, low Rb and high Sr all indicate being an amphibole.

Furthermore, the most volatile trace elements, Li, Rb, Pb and Bi, were measured in biotite, pyroxene, plagioclase and amphibole. Table 4.8 presents these concentrations for sample AP3, representing the layered cumulate rock, whereas the concentrations for sample AP7,

resembling a quenched liquid and hypothesized to have experienced eruptive degassing, are available in Table 4.9.

Table 4.8: Average volatile element concentrations (ppm) in biotite, pyroxene, plagioclase and amphibole in sample AP3 at the Mt. St. Grégoire intrusion

	Li7	**Rb85**	**Pb208**	**Bi209**
Biotite	80.00	609.17	1.53	0.03
Pyroxene	13.54	0.19	0.17	0.02
Plagioclase	1.06	4.91	2.57	0.01
Amphibole	23.03	11.01	1.46	0.04

Table 4.9: Average volatile element concentrations (ppm) in biotite, pyroxene and plagioclase in sample AP7 at the Mt. St. Grégoire intrusion

	Li7	**Rb85**	**Pb208**	**Bi209**
Biotite	43.8	507.1	1.8	0.03
Pyroxene	12.18	0.58	0.27	0.02
Plagioclase	1.46	4.90	3.23	0.02

Discussion

The Mt. St. Grégoire intrusion has been subject to various hypotheses explaining the rock type differentiation. The experimental approach used by Philpotts (1968) depended on two immiscible liquids convecting in a vertical pipe. He suggested that the gradation from a porphyritic syenite margin to an aphanitic gabbro core resulted from the crystallization of a convecting magma column which firstly separated into a syenitic magma and a gabbroic magma before the syenitic magma floated above due to a lower density. Eby (1979) also proposed an emplacement sequence using two immiscible liquids. He believed that the primitive magma was separated into two separate immiscible liquids to form the margin and transitional layered lithologies while the residual magma subsequently intruded through the centre of the conduit to produce the core. This hypothesis was determined by the partitioning of trace elements; the low-field strength elements were enriched in the silicic materials and the high-field strength elements were consequently enriched in the mafic materials, Eby (1979). Bédard (1989) interpreted the intrusion to have crystallized from a weakly convecting syenitic magma and have zoned from wall crystallization or liquid fractionation between this magma and rising, more primitive magmas. Contrasting Philpotts and Eby, Bédard also proposed that the transitional layered rocks are cumulates and do not represent immiscible liquid compositions. Regardless of the proposed emplacement model, the literature describes crystallization first occurring along the margins and progressing inwards towards the centre of the conduit along with the intrusion experiencing eruptive degassing to produce the aphanitic core surrounded by a porphyritic unit.

Evidence from Amphibole-Pyroxene Reaction Textures

The progressive decrease of amphibole in modal abundance and consequent increase of pyroxene from the margin to the core of the intrusion is demonstrated in Figure 4.2. This change in mineral assemblage along with the distinct reaction textures in Figure 4.3 have previously been presented as strong petrographical evidence of dehydration at Mt. St. Grégoire. However, dehydration of amphibole to pyroxene would be represented texturally by amphibole cores reacting to the surrounding pyroxene rims. On the contrary, observed across the intrusion are pyroxene cores progressively reacting to amphibole rims possibly due to the reaction:

pyroxene + plagioclase + water ↔ amphibole + silica (5)

Referring to Figure 4.3, AP7 and AP6 consist of unaltered pyroxene phenocrysts with amphibole nearly absent. AP5, AP4, AP3 and AP2 illustrate the progressive reaction of pyroxene to amphibole where AP5 shows large pyroxene cores with small amphibole reaction rims and AP2 shows small pyroxene cores with large amphibole reaction rims. AP1 appears as the most hydrated phase with stable amphibole phenocrysts and pyroxene nearly absent. Thus, what is occurring is the hydration of pyroxene to amphibole from the core to the margin of the intrusion, indicating an increase in water fugacity conditions in the same direction and not representing dehydration from degassing. The only petrographic evidence resulting from possible eruption at Mt. St. Grégoire is the aphanitic texture of sample AP7 resembling a quenched liquid (Figure 4.4C). However, this can also be explained by the core monzogabbro crystallizing at a high degree of undercooling due to the already-emplaced and cooled marginal porphyritic syenite. This high degree of undercooling would thus cause a high nucleation and consequently small crystals in the final intrusion event at the centre of the intrusion.

Evidence from Geothermobarometry Calculations

The oxygen fugacity values from Table 4.4 along with several magma type ranges are plotted in Figure 5.1. All the samples were measured to be reduced relative to NNO and range in ΔNNO from -1.41 to -2.04, corresponding in distribution to a reduced mid-ocean ridge basaltic (MORB) lava. The reduced state of the intrusion may also indicate having been generated in a depleted lithosphere. Figure 5.2 demonstrates the sequential range in ΔNNO across the intrusion. There are no apparent patterns amongst the samples and small variations in oxygen fugacity relative to each sample, thus it may be assumed that no significant redox changes occurred across the intrusion. Referring to Carmichael (1991), the range in Mt. St. Grégoire is also considerably reduced in comparison to his dataset of various lavas and ashflows ranging in ΔNNO from -3 to 5. He describes two relevant degassing situations, each having opposite effects on oxygen fugacity conditions. The first scenario involves the degassing of a submarine MORB naturally enriched in sulphur. Theoretically, the preferential evolution of SO_2 during eruption would remove oxygen from the ferric component in the melt and consequently result in a reduction, Carmichael (1991). While the samples are quite reduced, this can be ignored as the Mt. St. Grégoire intrusion was calculated to have crystallized 2-3km below surface and has no S-bearing mineral phases to confirm an initial enrichment in S. The alternative degassing method involves the reaction:

$$2FeO + H_2O \leftrightarrow Fe_2O_3 + H_2 \qquad (6)$$

This option assumes a water-saturated melt which is certainly possible in this study as per the above argument of pyroxene hydration to amphibole from the core to the margin of the intrusion. The primary issue is that although water is present, the reaction would produce Fe^{3+} during the

diffusive devolatilization of H_2 and cause oxidation, hence contradicting the measured reduced state of intrusion, Carmichael (1991). Therefore, while these opposing situations require different parameters to explain degassing, neither process can account for the major absence of S-bearing minerals or especially the negative ΔNNO values.

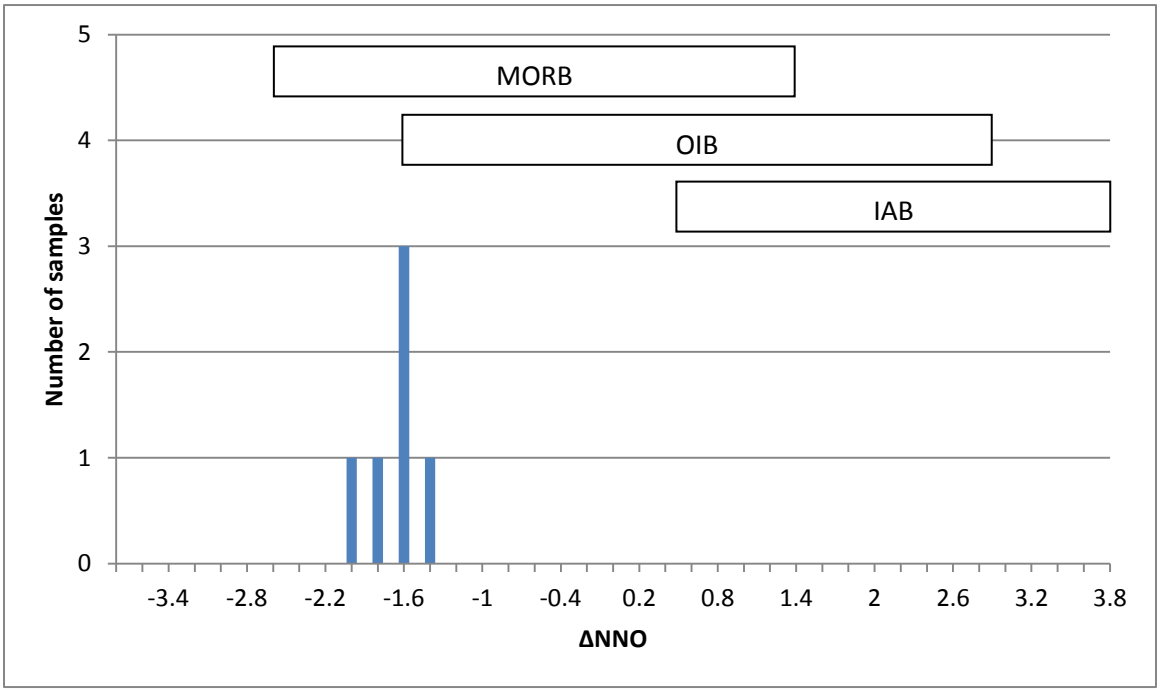

Figure 5.1: Graphical distribution of the log oxygen fugacity values relative to NNO of samples at the Mt. St. Grégoire intrusion. Mid-ocean ridge basalt (MORB), ocean island basalt (OIB) and island arc basalt (IAB) ranges are included for comparison, acquired from Mallmann and O'Neill (2007).

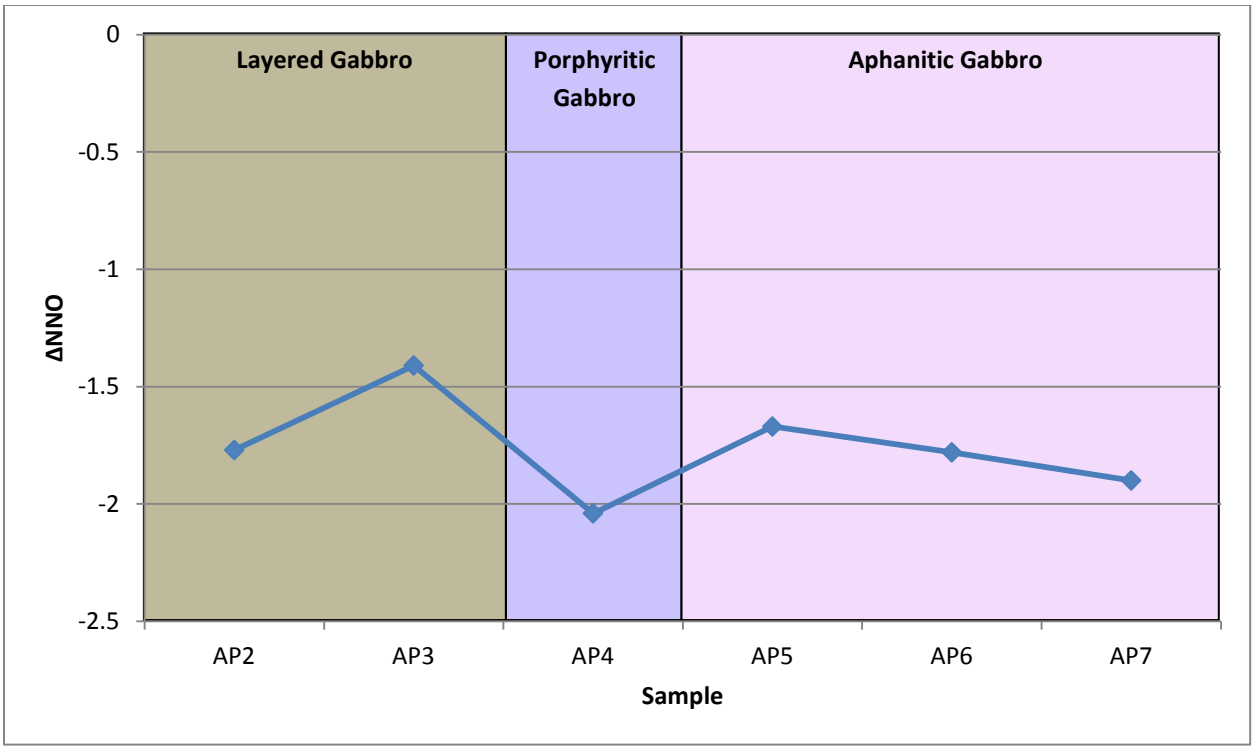

Figure 5.2: Graphical representation of the log oxygen fugacity values relative to NNO of samples at the Mt. St. Grégoire intrusion with no available error bars.

Evidence from Biotite Oxide Concentrations

Regarding Figure 4.8, MgO (purple) progressively decreases in abundance while FeO (green) significantly increases in abundance from the core to the margin of the intrusion. High values of $\frac{MgO}{MgO+FeO}$ as in sample AP7 are usually due to high temperature, early phase crystallization of the ferromagnesian minerals such as pyroxene and minor olivine. Simply based on these progressive compositional decreases and increases of MgO and FeO in biotite, respectively, one can infer these trend variations to result from natural differentiation of a primitive magma at the core to an evolved magma at the margin.

Using the oxide concentrations from Table 4.5 and an Excel biotite formula calculator created by Tindle and Webb (1990), the hydroxyl site atomic proportions between OH, F, and Cl were calculated and are presented in Table 5.1. Once the individual oxide concentrations were inputted into the spreadsheet, the molecular, cation and oxygen atomic proportions were calculated as well as the OH atomic proportion which was determined from the above weight percent values of F and Cl. Given Table 5.1, the OH component of the hydroxyl site progressively increases while F and Cl progressively decrease from the core to the margin of the intrusion. The main exception to these trends is sample AP1, perhaps as a result of its different, non-continuous lithology when compared to the core units of the intrusion. Regardless, the increase in OH provides further evidence of increasing water fugacity towards the margin, reinforcing the hydration texture of pyroxene to amphibole and validating the hypothesized increase of incompatible water from differentiation of a primitive magma from the centre of the intrusion outwards.

Table 5.1: Average hydroxyl site atomic proportions (%) in biotite at the Mt. St. Grégoire intrusion, calculated from Tindle and Webb (1990)

	AP1	**AP2**	**AP3**	**AP4**	**AP5**	**AP6**	**AP7**
OH	88.94	94.24	92.14	88.12	89.86	90.09	87.88
F	10.74	5.51	7.61	11.56	9.83	9.59	11.68
Cl	0.33	0.26	0.25	0.31	0.31	0.31	0.44

Moreover, the decreasing amount of OH in biotite in the aphanitic monzogabbro unit is not explained by eruption. F and Cl behave differently as volatile elements; the partition coefficient between the aqueous fluid and the melt for F is much less than 1 and for Cl is 10±1.5,

Villemant and Boudon (1999). Thus, Cl would readily leave the system during degassing which would also be reflected in the biotite structure. A significant decrease in concentration would be expected if the intrusion had experienced devolatilization, however, the atomic proportion of Cl increases from AP3 to AP7. Hence, Cl in this study can solely provide definite evidence opposing degassing at Mt. St. Grégoire. Additionally, multiple variations in hydroxyl site atomic proportions are shown in Figure 5.3 where the blue lines represent the actual variation in biotite. Assuming very minor and localized degassing in the aphanitic monzogabbro without affecting the water content, sample AP7 would theoretically have higher F around 12% and a conservatively small decrease in Cl from 0.44% to 0.11%. Considering the massive influence of eruption on Cl partitioning, the decreased Cl concentrations would cause the variation trends to dramatically increase (in red; interpretation and not modelled) although the opposite is observed. The alternative approach to strongly argue against degassing of the core is to plot the variation in Cl and F concentration in the melt along the intrusion as in Figure 5.4. While the Cl content of the melt may be changing, the partitioning coefficient for Cl in the melt also varies as a function of biotite composition. Hence, calculating the χ_{Mg} from Table 4.5 and using the linear regression equations determined from the partition coefficients for F and Cl provided by Chevychelov et al. (2008) will allow the calculation of Cl and F content in the coexisting melt. Figure 5.4A illustrates the systematic increase in Cl concentration in the melt towards the core of the intrusion where AP7 has the highest Cl content in the melt; hypothetically though, AP7 should be the most depleted in volatile Cl from the melt if the centre experienced eruption and Cl readily left the system. For instance, the red numbers represent increasing amounts of degassed fluid. Point 2 demonstrates a loss of 3% fluid and corresponds to 0.213% Cl in the melt which is 0.054% less than undegassed AP6 and considerably lower than AP7. Excluding the margins as a

different rock type in Figure 5.3B, F content in the coexisting melt is approximately constant across Mt. St. Grégoire as expected from its small partition coefficient.

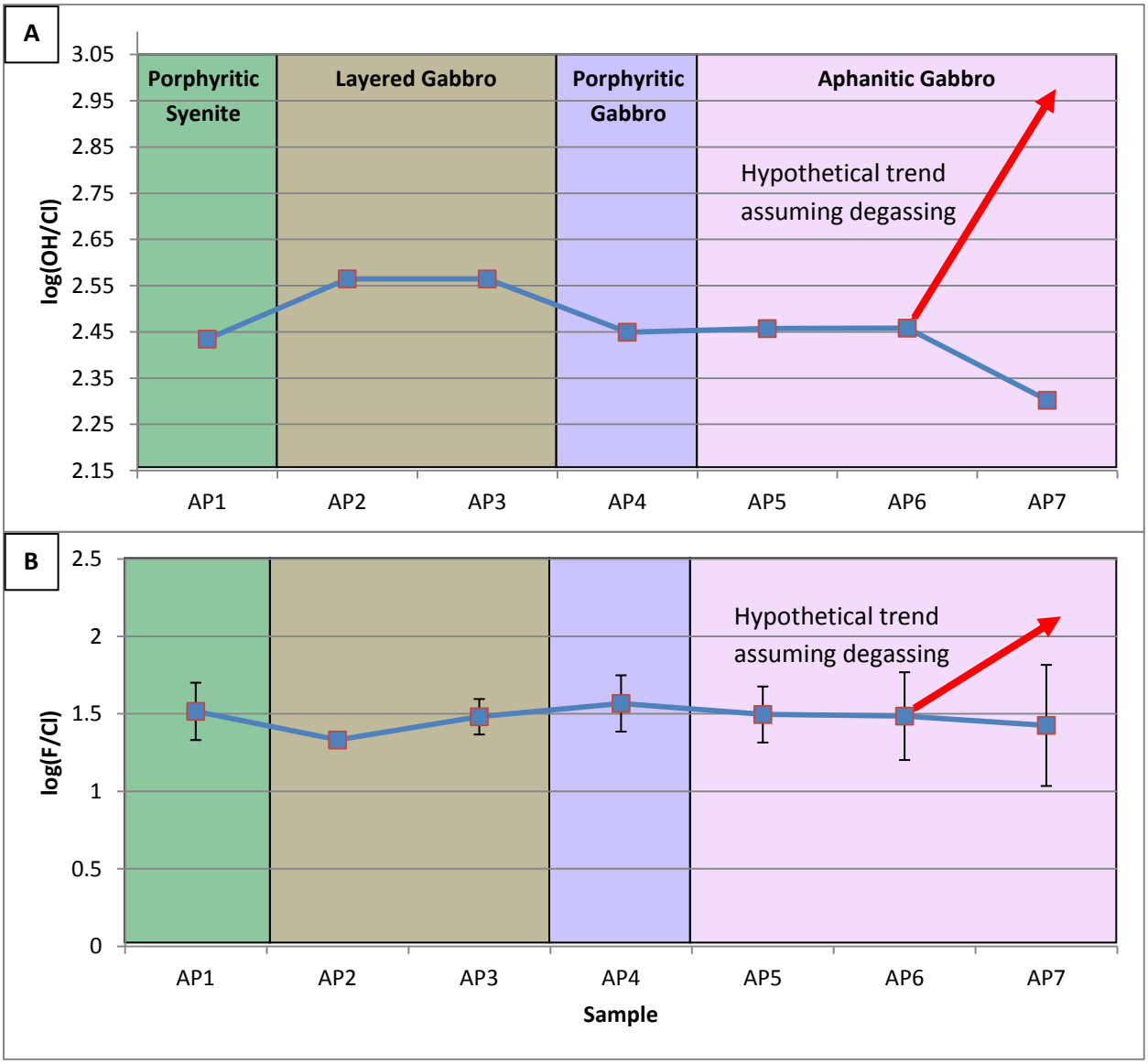

Figure 5.3: Graphical representation of the hydroxyl site atomic proportion trends in biotite at the Mt. St. Grégoire intrusion. The blue lines represent the actual measured variation and the red lines represent the theoretical, non-modelled variation assuming AP7 %F = 12, %Cl = 0.11. A: Variation in log(OH/Cl) with no available error bars. B: Variation in log(F/Cl) with 1σ error bars.

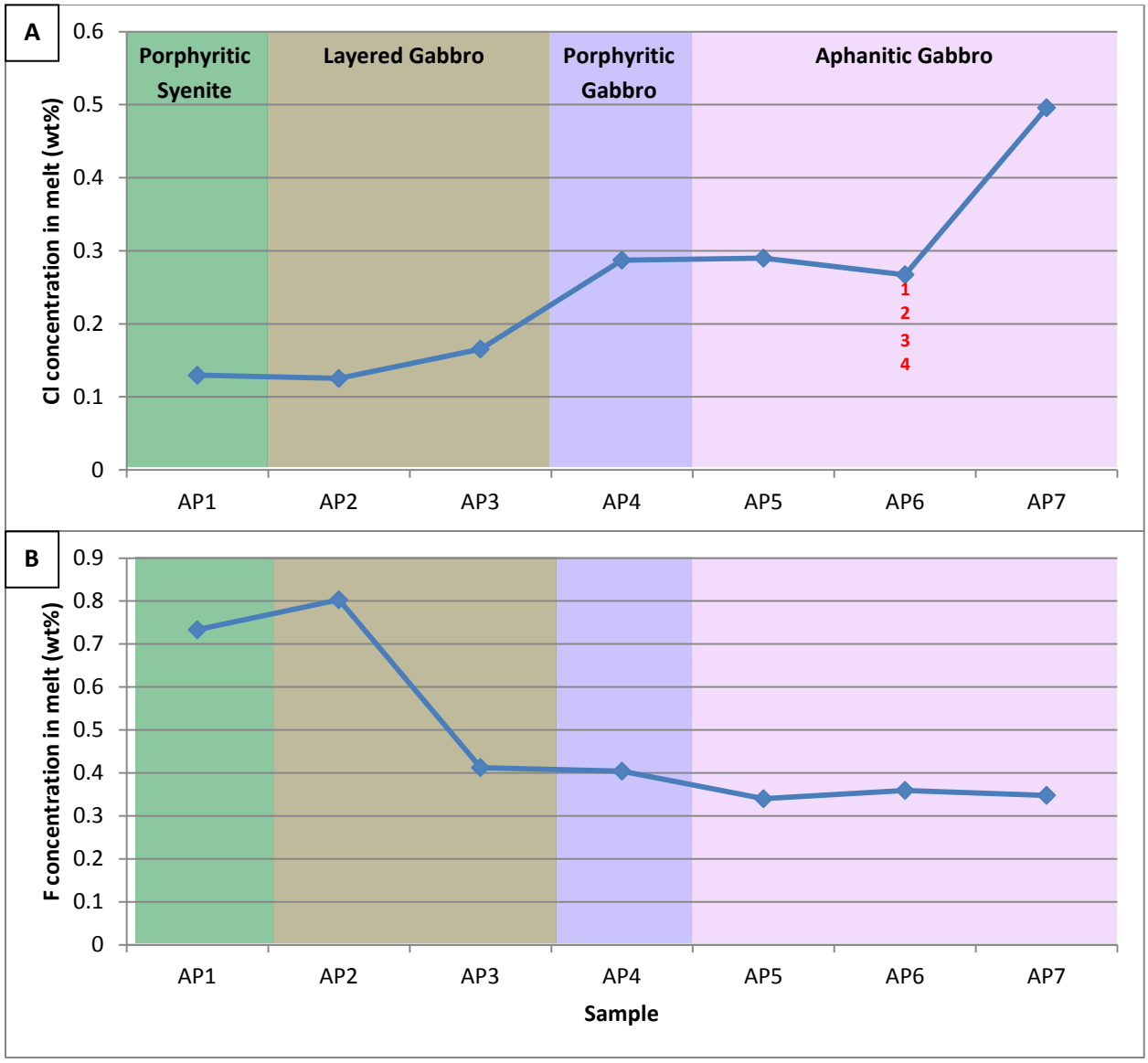

Figure 5.4: Graphical representation of the concentration trends for halogen elements in the melt at the Mt. St. Grégoire intrusion with no available error bars. A: Variation in Cl in the melt. Point 1 represents degassing of $\chi_{fluid} = 1\%$. Point 2 represents degassing of $\chi_{fluid} = 3\%$. Point 3 represents degassing of $\chi_{fluid} = 5\%$. Point 4 represents degassing of $\chi_{fluid} = 10\%$. B: Variation in F in the melt.

Evidence from Apatite and Biotite Trace Element Concentrations

The concentration trends of several REEs, Th and U in apatite are given in Figure 4.9. Apatite is the earliest phase to crystallize in all samples (Figure 4.3) and the only mineral phase in the assemblage which will easily accommodate REEs, Th and U from the melt and thus represents a general behaviour for these elements across the intrusion. Furthermore, these trace elements are all compatible in apatite, Watson and Green (1981), Bea et al. (1994). Since the REEs, Th and U will more readily partition into the mineral than into the residual melt, the primitive rock type is expected to have the largest concentration of these elements with a progressive decrease in consequent units corresponding to sequences of more evolved magmas. Generally, these concentrations decrease in abundance from the core to the margin of the intrusion, possibly relating to magma differentiation from the centre outwards. Sample AP1, however, is the most enriched in each of the above trace elements, once more possibly due to its different lithology with no proper geologic continuity across the entire intrusion.

Similarly, Figure 4.10 demonstrates the concentrations of Rb, Li and Cu in biotite across Mt. St. Grégoire. Overall, Rb (green) is slightly increasing from the centre to the margin. This Re trend is hypothesized to be from differentiation of a primitive magma at the core to an evolved magma at the margin as previously discussed where Re is enriched in progressively more felsic zones. Li is a volatile and incompatible element in biotite, Brenan et al. (1998), thus is expected to remain in the residual melt and progressively increase in concentration with each sample towards the margin just as observed in Figure 4.10. Conversely, Cu is a highly compatible element, Ewart and Griffin (1994), and decreases in concentration from the core to the margin as less available Cu gradually partitions into biotite in more evolved rocks.

Evidence from Volatile Element Concentrations

Referring to the described behaviour of Li in biotite, the same fractionation process can be considered for the variation of other incompatible elements along the intrusion. Table 4.8 and Table 4.9 present volatile trace element concentrations for several minerals in AP3 and AP7, respectively. Assuming the observed pattern of a primitive to evolved magma from the core outwards, all incompatible volatile elements should preferentially partition into the residual melt and increase in concentration from the centre to the margin. Theoretically, the mineral phases in AP7 would have the lowest concentrations of volatile elements as they are mainly partitioning into the primitive melt. Consequent samples such as AP3 would have higher concentrations compared to AP7 as they would crystallize from already-fractionated, incompatible volatile element-enriched residual melt. This concept can be calculated in detail. Firstly, the mineral modal abundances listed in Table 4.1 must be converted to mass fractions using their respective densities, acquired from The Engineering Toolbox (2013). Secondly, each mass fraction and volatile element concentration can be combined to determine the total mineral volatile content in the sample for comparison.

AP7 volatile element-containing mineral modal abundance to mass fraction conversions:

$$\chi_{\text{bio}} = \frac{\left(\frac{3.2\text{g}}{\text{cm}^3}\right)(\sqrt{0.01})^3}{\left(\frac{3.2\text{g}}{\text{cm}^3}\right)(\sqrt{0.01})^3 + \left(\frac{3.4\text{g}}{\text{cm}^3}\right)(\sqrt{0.12})^3 + \left(\frac{2.67\text{g}}{\text{cm}^3}\right)(\sqrt{0.7})^3}$$

$$\text{Biotite mass fraction} = \chi_{\text{bio}} = 0.0019$$

$$\chi_{\text{pyr}} = \frac{\left(\frac{3.4\text{g}}{\text{cm}^3}\right)(\sqrt{0.12})^3}{\left(\frac{3.2\text{g}}{\text{cm}^3}\right)(\sqrt{0.01})^3 + \left(\frac{3.4\text{g}}{\text{cm}^3}\right)(\sqrt{0.12})^3 + \left(\frac{2.67\text{g}}{\text{cm}^3}\right)(\sqrt{0.7})^3}$$

Pyroxene mass fraction $= \chi_{pyr} = 0.083$

$$\chi_{plag} = \frac{\left(\frac{2.67\text{g}}{\text{cm}^3}\right)(\sqrt{0.7})^3}{\left(\frac{3.2\text{g}}{\text{cm}^3}\right)(\sqrt{0.01})^3 + \left(\frac{3.4\text{g}}{\text{cm}^3}\right)(\sqrt{0.12})^3 + \left(\frac{2.67\text{g}}{\text{cm}^3}\right)(\sqrt{0.7})^3}$$

Plagioclase mass fraction $= \chi_{plag} = 0.92$

AP7 total mineral volatile element concentrations:

$$C_{min}^{Li} = \chi_{bio} C_{bio}^{Li} + \chi_{pyr} C_{pyr}^{Li} + \chi_{plag} C_{plag}^{Li}$$

$$C_{min}^{Li} = (0.0019)(43.8\text{ppm}) + (0.083)(12.18\text{ppm}) + (0.92)(1.46\text{ppm}) = \mathbf{2.44ppm}$$

$$C_{min}^{Rb} = \chi_{bio} C_{bio}^{Rb} + \chi_{pyr} C_{pyr}^{Rb} + \chi_{plag} C_{plag}^{Rb}$$

$$C_{min}^{Rb} = (0.0019)(507.1\text{ppm}) + (0.083)(0.58\text{ppm}) + (0.92)(4.90\text{ppm}) = \mathbf{5.52ppm}$$

$$C_{min}^{Pb} = \chi_{bio} C_{bio}^{Pb} + \chi_{pyr} C_{pyr}^{Pb} + \chi_{plag} C_{plag}^{Pb}$$

$$C_{min}^{Pb} = (0.0019)(1.8\text{ppm}) + (0.083)(0.27\text{ppm}) + (0.92)(3.23\text{ppm}) = \mathbf{3.00ppm}$$

AP3 volatile element-containing mineral modal abundance to mass fraction conversions:

$$\chi_{bio} = \frac{\left(\frac{3.2\text{g}}{\text{cm}^3}\right)(\sqrt{0.08})^3}{\left(\frac{3.2\text{g}}{\text{cm}^3}\right)(\sqrt{0.08})^3 + \left(\frac{3.4\text{g}}{\text{cm}^3}\right)(\sqrt{0.05})^3 + \left(\frac{2.67\text{g}}{\text{cm}^3}\right)(\sqrt{0.65})^3 + \left(\frac{3.22\text{g}}{\text{cm}^3}\right)(\sqrt{0.1})^3}$$

Biotite mass fraction $= \chi_{bio} = 0.045$

$$\chi_{pyr} = \frac{\left(\frac{3.4\text{g}}{\text{cm}^3}\right)(\sqrt{0.05})^3}{\left(\frac{3.2\text{g}}{\text{cm}^3}\right)(\sqrt{0.08})^3 + \left(\frac{3.4\text{g}}{\text{cm}^3}\right)(\sqrt{0.05})^3 + \left(\frac{2.67\text{g}}{\text{cm}^3}\right)(\sqrt{0.65})^3 + \left(\frac{3.22\text{g}}{\text{cm}^3}\right)(\sqrt{0.1})^3}$$

Pyroxene mass fraction $= \chi_{pyr} = 0.024$

$$\chi_{plag} = \frac{\left(\frac{2.67g}{cm^3}\right)(\sqrt{0.65})^3}{\left(\frac{3.2g}{cm^3}\right)(\sqrt{0.08})^3 + \left(\frac{3.4g}{cm^3}\right)(\sqrt{0.05})^3 + \left(\frac{2.67g}{cm^3}\right)(\sqrt{0.65})^3 + \left(\frac{3.22g}{cm^3}\right)(\sqrt{0.1})^3}$$

Plagioclase mass fraction $= \chi_{plag} = 0.87$

$$\chi_{amp} = \frac{\left(\frac{3.22g}{cm^3}\right)(\sqrt{0.1})^3}{\left(\frac{3.2g}{cm^3}\right)(\sqrt{0.08})^3 + \left(\frac{3.4g}{cm^3}\right)(\sqrt{0.05})^3 + \left(\frac{2.67g}{cm^3}\right)(\sqrt{0.65})^3 + \left(\frac{3.22g}{cm^3}\right)(\sqrt{0.1})^3}$$

Amphibole mass fraction $= \chi_{amp} = 0.063$

AP3 mineral total volatile element concentrations (shortened):

$C_{min}^{Li} = \chi_{bio}C_{bio}^{Li} + \chi_{pyr}C_{pyr}^{Li} + \chi_{plag}C_{plag}^{Li} + \chi_{amp}C_{amp}^{Li}$

$C_{min}^{Li} = 3.6ppm + 0.32ppm + 0.92ppm + 1.45ppm = \mathbf{6.29ppm}$

$C_{min}^{Rb} = \chi_{bio}C_{bio}^{Rb} + \chi_{pyr}C_{pyr}^{Rb} + \chi_{plag}C_{plag}^{Rb} + \chi_{amp}C_{amp}^{Rb}$

$C_{min}^{Rb} = 27.41ppm + 0.0046ppm + 4.27ppm + 0.69ppm = \mathbf{32.38ppm}$

$C_{min}^{Pb} = \chi_{bio}C_{bio}^{Pb} + \chi_{pyr}C_{pyr}^{Pb} + \chi_{plag}C_{plag}^{Pb} + \chi_{amp}C_{amp}^{Pb}$

$C_{min}^{Pb} = 0.069ppm + 0.0041ppm + 2.23ppm + 0.092ppm = \mathbf{2.4ppm}$

Sample AP3 appears to be generally enriched in volatile elements as theoretically proposed. Li and especially Rb increased in concentration from sample AP7 while Pb is constant. Bi was excluded from the calculations as concentration measurements were below analytical uncertainty. Lastly, this simple computation offered additional confirmation on the increase in concentration trends of volatile incompatible elements at the Mt. St. Grégoire intrusion from natural differentiation, evolution and fraction of melt from the core unit to the marginal series.

Conclusion

In summary, there is strong geochemical and textural evidence opposing the degassing hypothesis at the Mt. St. Grégoire intrusion. Petrographically, the distinct reaction textures support hydration of pyroxene to amphibole from the core to the margin of the intrusion, indicating an increase in water fugacity conditions in the same direction rather than dehydration towards the centre. The Fe-Ti oxide geothermobarometry calculations resulted in a small scattered logfO_2 range between ΔNNO -1.44 and -2.04. The two relevant degassing situations proposed by Carmichael (1991) were disproved on the basis of each scenario contradicting other fundamental observations. Regarding biotite, the progressive decrease of $\frac{\mathrm{MgO}}{\mathrm{MgO+FeO}}$ from the core unit to the margin can be explained by the natural differentiation of a primitive magma at the core to an evolved magma at the margin. Furthermore, hydroxyl site atomic proportions demonstrated the relatively consistent behaviour of F along the intrusion. Considering the high partition coefficient between the aqueous fluid and the melt for Cl, degassing would certainly be detectable in the variation between Cl and F or Cl and OH as well as in Cl content in the coexisting melt. However, the lack of decrease in Cl, especially its enrichment at the core, can solely provide definite evidence opposing degassing at Mt. St. Grégoire which is illustrated in the reinterpreted emplacement model in Figure 5.5. Generally, the original model proposed by Bédard (1989) is accepted except for the degassing hypothesis replaced by crystallization at a high degree of undercooling to account for the aphanitic texture in the core. Additionally, the compatible trace elements in apatite and biotite progressively decrease in abundance while volatile incompatible elements progressively increase in abundance from the core to the margin; further supporting the possibility of Mt. St. Grégoire crystallizing from a late intruded primitive aphanitic monzogabbro at the core and progressively more evolved lithologies to the nepheline

syenite along the margins. Finally, future research in apatite textures, ulvöspinel and ilmenite textures as well as in the detailed partitioning behaviour of trace and volatile elements for numerous minerals will all provide supplementary data for further interpretation of the geology and nature of this interesting intrusion.

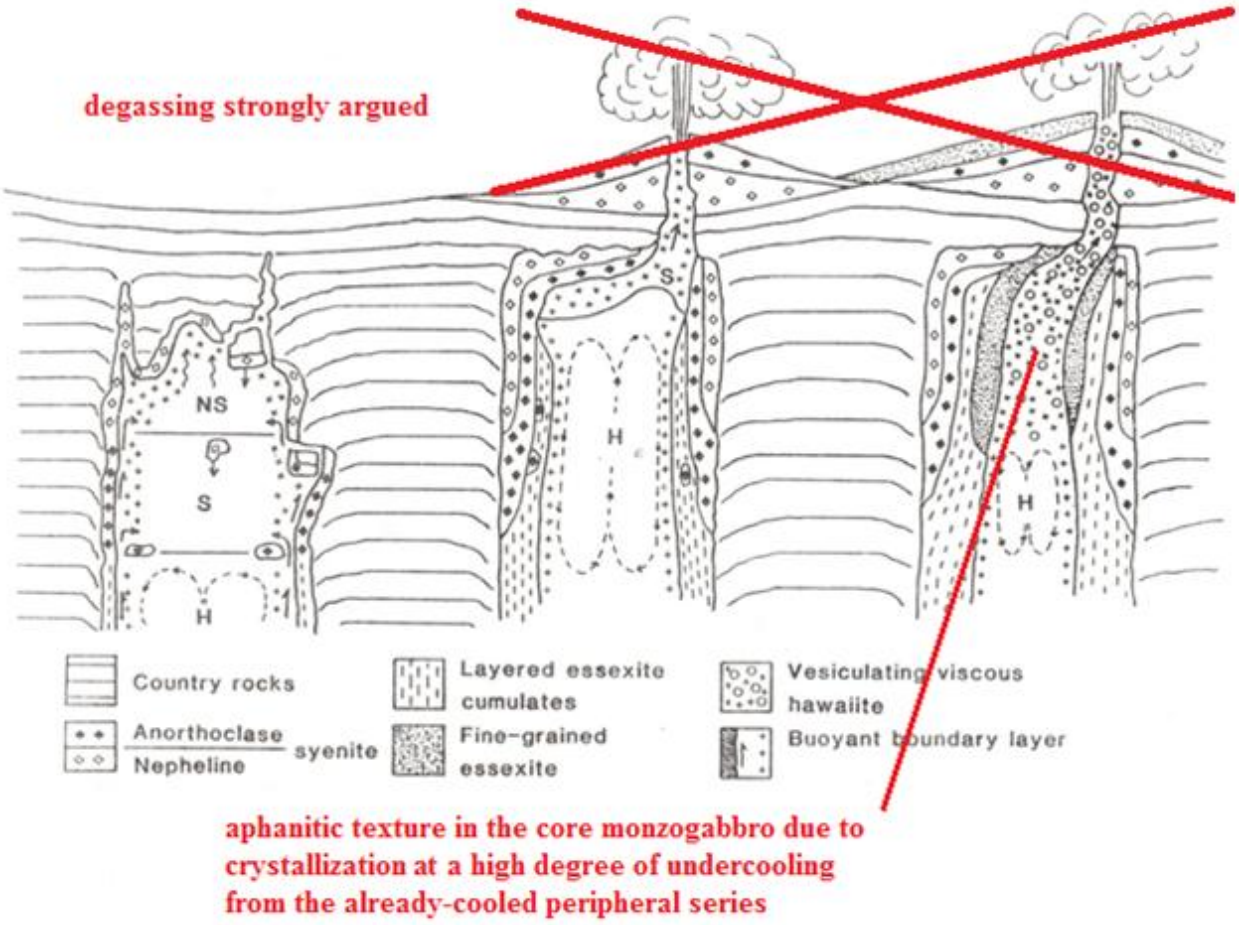

Figure 5.5: Revised interpretative emplacement model for the Mt. St. Grégoire intrusion, modified from Bédard (1989).

Acknowledgments

I am grateful to Professor James Brenan for his guidance, support and constructive reviews. I thank George Kretschmann, Colin Bray, Boris Foursenko and Bohdan Podstawskyj for their technical assistance with the analytical equipment and sample preparation. This research was supported by the Department of Earth Sciences at the University of Toronto.

References

Bea, F., Pereira, M.D., Stroh, A. (1994) Mineral/leucosome trace-element partitioning in a peraluminous migmatite (a laser ablation-ICP-MS study). Chemical Geology, vol 117, pp291-312.

Bédard, J.H. (1989) The Monteregian Hills and White Mountain magma series: a field guide to the Sainte Dorothée sill and Mounts Royal, Johnson and Mégantic. GAC MAC Field Guide B3, pp29-106.

Brenan, J.M., Neroda, E., Lundstrom, C.C., Shaw, H.F., Ryerson, F.J., Phinney, D.L. (1998) Behaviour of boron, beryllium, and lithium during melting and crystallization: Constraints from mineral-melt partitioning experiments. Geochimica et Cosmochimica Acta, vol 62, pp2129-2141.

Chevychelov, V.Y., Botcharnikov, R.E., Holtz, F. (2008) Experimental Study of Fluorine and Chlorine Contents in Mica (Biotite) and Their Partitioning between Mica, Phonolite Melt, and Fluid. Geochemistry International, vol 46, pp1081-1089.

Eby, G.N. (1979) Mount Johnson, Quebec – An example of silicate-liquid immiscibility? Geology, vol 7, pp491-494.

Eby, G.N. (1984) Monteregian Hills I. Petrography, Major and Trace Element Geochemistry, and Strontium Isotopic Chemistry of the Western Intrusions: Mounts Royal, St. Bruno and Johnson. Journal of Petrology, vol 25, pp421-452

Ewart, A., Griffin, W.L. (1994) Application of Proton-Microprobe Data to Trace-Element Partitioning in Volcanic-Rocks. Chemical Geology, vol 117, pp251-284.

Ghiorso, M.S., Evans, B.W. (2008) Thermodynamics of Rhombohedral Oxide Solid Solutions and a Revision of the Fe-Ti Two-oxide Geothermometer and Oxygen-barometer. American Journal of Science, vol 308, pp957-1039.

Hauri, E.H., Wagner, T.P., Grove, T.L. (1994) Experimental and natural partitioning of Th, U, Pb and other trace elements between garnet, clinopyroxene and basaltic melts. Chemical Geology, vol 117, pp149-166.

Johnson, A., Canil, D. (2011) The degassing behavior of Au, Tl, As, Pb, Re, Cd and Bi from silicate liquids: Experiments and applications. Geochimica et Cosmochimica Acta, vol 75, pp1773-1784.

MacKenzie, J.M., Canil, D. (2011) Fluid/melt partitioning of Re, Mo, W, Tl and Pb in the system haplobasalt-H_2O-Cl and the volcanic degassing of trace metals. Journal of Volcanology and Geothermal Research, vol 204, pp57-65.

Mallmann, G., O'Neill, H.S.C. (2007) The effect of oxygen fugacity on the partitioning of Re between crystals and silicate melt during mantle melting. Geochimica et Cosmochimica Acta, vol 71, pp2837-2857.

Philpotts, A.R. (1968) Igneous structures and mechanism of emplacement of Mount Johnson, a Monteregian intrusion, Quebec. Canadian Journal of Earth Sciences, vol 5, pp1131-1137.

Roulleau, E., Pinti, D.L., Stevenson, R.K., Takahata, N., Sano, Y., Pitre, F. (2012) N, Ar and Pb isotopic co-variations in magmatic minerals: Discriminating fractionation processes from magmatic sources in Monteregian Hills, Québec, Canada. Chemical Geology, vol 326-327, pp121-131.

Rubin, K. (1997) Degassing of metals and metalloids from erupting seamount and mid-ocean ridge volcanoes: Observations and predictions. Geochimica et Cosmochimica Acta, vol 61, pp3525-3542.

Tindle, A.G., Webb, P.C. (1990) Estimation of lithium contents in trioctahedral micas using microprobe data: application to micas from granitic rocks. European Journal of Mineralogy, vol 2, pp595-610.

Unknown (2013) Densities of common minerals. The Engineering Toolbox. Retrieved on March 30, 2013, from http://www.engineeringtoolbox.com/mineral-density-d_1555.html

Villemant, B., Boudon, G. (1999) H_2O and halogen (F, Cl, Br) behaviour during shallow magma degassing processes. Earth and Planetary Science Letters, vol 168, pp271-286.

Watson, E.B., Green, T.H. (1981) Apatite/liquid partition coefficients for the rare earth elements and strontium. Earth and Planetary Science Letters, vol 56, pp405-421.